2006

AN INTELLIGENT SYSTEM FOR THE DEFECT INSPECTION OF SPECULAR PAINTED CERAMIC TILES

JINHUA LI
University of Kentucky, li31@purdue.edu

Recommended Citation

LI, JINHUA, "AN INTELLIGENT SYSTEM FOR THE DEFECT INSPECTION OF SPECULAR PAINTED CERAMIC TILES" (2006). *University of Kentucky Master's Theses*. 355.
https://uknowledge.uky.edu/gradschool_theses/355

AN INTELLIGENT SYSTEM FOR THE DEFECT INSPECTION OF SPECULAR PAINTED CERAMIC TILES

JINHUA LI

NOVEMBER 2005

ABSTRACT OF THESIS

AN INTELLIGENT SYSTEM FOR THE DEFECT INSPECTION OF SPECULAR PAINTED CERAMIC TILES

Product visual inspection is still performed manually or semi automatically in most industries from simple ceramic tile grading to complicated automotive body panel paint defect and surface quality inspection. Moreover, specular surfaces present additional challenges to conventional vision systems due to specular reflections, which may mask the true location of objects and lead to incorrect measurements. Some sophisticated optical inspection methods have already been developed for high precision surface defect inspection in recent years. Unfortunately, most of them are highly computational. Systems built on those methods are either inapplicable or costly to achieve real-time inspection. This thesis describes an integrated low-cost intelligent system developed to automatically capture and extract regular defects of the ceramic tiles with uniformly colored specular coatings. The proposed system is implemented on a group of smart cameras using its on-board processing ability to achieve real-time inspection. The results of this study will be used to facilitate the design of a robust, low-cost, closed-loop inspection system for a class of products with smooth specular coatings. The experimental results on real test panels demonstrate the effectiveness and robustness of proposed system.

KEYWORDS: Specular Surface, Defect Inspection, Real-Time Inspection, Intelligent System, System Integration

Jinhua Li

November 31, 2005

AN INTELLIGENT SYSTEM FOR THE DEFECT INSPECTION OF SPECULAR PAINTED CERAMIC TILES

By

Jinhua Li

Dr. Johné M. Parker
Director of Thesis

Dr. George Huang
Director of Graduate Studies

THESIS

Jinhua Li

The Graduate School

University of Kentucky

2005

AN INTELLIGENT SYSTEM FOR THE DEFECT INSPECTION OF SPECULAR PAINTED CERAMIC TILES

THESIS

A thesis submitted in partial fulfillment of the requirements
for the degree of Master of Science in Mechanical
Engineering at the University of Kentucky

By

Jinhua Li

Director: Dr. Johné M. Parker, Associate Professor
Lexington, Kentucky

2005

MASTER'S THESIS RELEASE

I authorize the University of Kentucky Libraries to reproduce this thesis in whole or in part for purposes of research.

Signed: ______________________________
Date: ________________________________

ACKNOWLEDGEMENTS

This is to my parents.

Thanks to my advisor, Dr. Johné M. Parker. You open the door for my future.

Thanks to Dr. Yumin Zhang and Dr. Scott Stephens to serve on my committee.

Thanks to all my friends and colleagues.

TABLE OF CONTENTS

CHAPTER 1

INTRODUCTION

CHAPTER 2

THEORY BACKGROUND AND RELATED WORK

CHAPTER 3

PAINT SURFACE DEFECTS AND THEIR MATHEMATICAL MODELING

CHAPTER 4

APPARATUS SELECTION AND EXPERIMENT TESTBED SETUP

CHAPTER 5

DEFECT DETECTION AND FEATURE EXTRACTION

CHAPTER 6

INSPECTION IMPLEMENTATION

CHAPTER 7

RESULTS AND DISCUSSION

CHAPTER 8

CONCLUSIONS AND FUTURE WORK

APPENDIX: A

INTRODUCTION OF SMARTIMAGE INTELLIGENT SENSOR

APPENDIX: B

APPENDIX: C

LIST OF TABLES

LIST OF FIGURES

CHAPTER 1

INTRODUCTION

1.1 Motivation

The inspection of a product's specular surface is important in many maintenance tasks, and also in many industrial production processes. There are industrial applications that range from simple ceramic tile grading to complicated automotive body panel defect detection and surface quality inspection. Such applications are important since, not only can a well coated finish enhance the durability by protecting the product surface for corrosion, but surface appearance is a key factor in the product's quality [1]. It has a direct impact on the customer's initial buying decision. There is a long-standing desire in many industries to replace the current labor-based visual inspection of a product with machine-based inspection. These types of inspection systems are generally implemented to facilitate a more robust and faster inspection, as well as to provide feedback to the coating process. For example, the ceramic tile industry has taken significant advantages of the advances in the world of automation in recent years. All production phases have been addressed through various technical innovations, with the exception of the final manufacturing stage concerned with the product's visual inspection, which is still performed manually. Expert inspectors are hired in the plant to inspect defects and assess the color, gloss etc. in order to monitor surface quality. Though such an inspection method is effective, it is costly and labor intensive. More importantly, the results presented by individual human inspectors can be subjective and inconsistent due to unavoidable human errors. For many years, researchers from both industrial and academic institutions have been conducting research on relevant topics [2]. However, the tasks of inspection on the specular surfaces are still challenging today. Several major problems are still under study:

- First, it must be better understood how to efficiently extract and measure three-dimensional shapes from the specular surface. Such surfaces present a challenge to conventional vision systems due to specular reflections, which may mask the true location of objects and lead to incorrect measurements. A primary goal of such measurements is to convert two-dimensional image data to a three dimensional shape measurement of an object, e.g. body panel paint defect and dent inspection. These all involve the analysis of images resulting from the reflection of light.

- Another important problem is the actual industrial inspection system design and real-time implementation. Currently, a high precision surface inspection technology, such as phase reflectance [18], has already been able to extract and measure surface faults as small as a micrometer in depth. However, the complicated algorithms and strict experimental conditions that must generally be used to obtain the necessary data suggest that this technology is not yet applicable for industrial real time mass product inspection. Also available is a commercial on-line quality inspection system for real time surface inspections, as discussed in section 2.3. Not only is it expensive, but it is designed for only a specific industrial inspection task. So it focuses only on a certain aspect of the paint appearance.
- The overall paint appearance is a function of multiple parameters. Defects are one aspect. It is also linked to gloss, color, texture, etc. Moreover, the link between the measured paint quality parameters and the customer's initial impressions of the overall quality of the product is still not well understood.

This thesis addresses a subset of the first two problems related to the specific application of real-time surface defect inspection of ceramic tiles. As opposed to the automobile industry, the ceramic tile industry is low-cost and low-profit. However, the quality of each ceramic tile still needs to meet certain guidelines as well as minimum surface quality performance levels established by the American National Standards Institute (ANSI) together with the American Society of Testing and Materials (ASTM) [3]. In order to replace the current labor-based surface quality visual inspection while controlling the production cost, an integrated low-cost intelligent system is developed to automatically capture images, detect regular geometric defects, and extract their features on specular coated ceramic tiles. The results suggest that the performance of this integrated system is adequate to provide a basis for a viable commercial visual inspection system. Furthermore, the results of this investigation can be easily extended to suggest effective designs for inspecting a class of smooth specular coatings, such as those often present on appliances and automobiles.

1.2 Problem Statement

Figure 1.1 provides a simple schematic of a proposed long term objective in the machine vision group at the Mechanical Engineering Department, University of Kentucky. This long-term research objective contributes to advancements in the design of robust low-cost intelligent systems for real-time inspection of smooth specular coatings. In this investigation, the primary defects studied are seed defects and spot defects. This is because they are the common surface defects found on real ceramic tiles and present as irregular shapes and different sizes. Image processing algorithms for defect detection and feature extraction are proposed and executed on a group of smart cameras using their on-board processing ability. Finally, an integrated small-scale low-cost experimental testbed is developed for the real-time implementation of proposed algorithms.

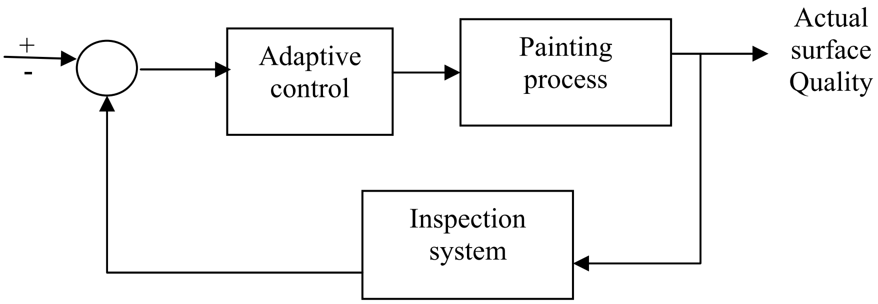

Figure 1.1 an automated Defect Detection system with feedback control

1.3 Thesis Outline

The remainder of this thesis is organized as follows: Chapter Two presents a literature review on the theory of surface physical reflectance, available methods for the specular surface inspection, as well as several existing quality inspection systems. In Chapter Three, a Gaussian curve is used to model seed defects, with the support function representation. Then this defect model is used to analyze the surface specular reflection around the defect area in order to explain the defect inspection mechanisms via specular reflections in the experiment system. Chapter Four describes the experiment testbed structure and setup, which includes the experiment light source, camera selection and software design. Image processing algorithms used for defect detection and feature extraction in this experiment are addressed in Chapter Five. Chapter Six discusses the details of inspection implementation. Chapter Seven presents and discusses the experimental results. Chapter Eight contains the conclusion, and recommendations for future work.

CHAPTER 2

THEORY BACKGROUND AND RELATED WORK

Optical methods are used to analyze surface quality in this investigation; therefore, all the surface inspection technologies presented in this chapter analyze information gathered from the light rays reflected from the inspection product surface. Section 2.1 first discusses some of the most important results related to the modeling of surface physical reflectance. Nayar's unified reflectance framework is well recognized as one of most accurate surface physical reflection models and provides the scientific based for this study;, its details are introduced at the end of this section. Although information derived from specular highlights may be useful, specular painted ceramic tile surfaces may present highlights due to specular reflections that mask the true location of objects and lead to incorrect measurements. Section 2.2 discusses some latest inspection methods on such specular surfaces. In Section 2.3, some current available on-line paint quality inspection systems are discussed and compared with the experiment system in this study.

2.1 Surface physical reflection models

Some earlier approaches to surface physical reflection models [4] [5] [6] have assumed that the surfaces are Lambertian [7], in which the incident light is scattered by the surface evenly around the surface normal direction. However, an ability to understand specular features is valuable for any vision system, which must interpret images of glossy surfaces; e.g. a specular highlight can yield additional information about the local curvature of the surface. So it can be used to resolve convex or concave ambiguities.

Later representative research studies on this subject include Phong [8], who proposed a parameterized continuous function to represent specular reflectance and used it to create images of the objects; Ikeuchi [9] and Sanderson [10] used the double-delta specular model to determine the shape of specular surfaces by a photometric stereo and structured highlight technique; Healey and Binford [11] used the Torrance-Sparrow model [12] to analyze monocular images to estimate local shape curvature.

Based upon those earlier approaches, Nayar [13] proposes a more accurate unified reflectance framework for the machine vision that predicts the reflectance of monochromatic light from both smooth and rough surfaces. It is based on both geometrical and physical reflectance models. The new model consists of three primary reflectance components: the specular lobe, the specular spike, and the diffuse lobe as shown in Figure 2.1. The specular spike is dominant on smooth glossy surfaces. It is concentrated in a small region around the specular, or mirror, direction. The specular lobe is distributed around the specular direction and has an off-specular peak for rough surfaces. The magnitudes of both the specular lobe and the specular spike components are determined by surface properties, such as roughness. The specular spike is dominant on a highly smooth surface. As the surface roughness increases, the spike component shrinks rapidly and the specular lobe starts dominating. Moreover, away from the specular direction, both magnitudes decrease drastically and minimal light energy is reflected. Finally, the Lambertian model is used to represent the diffuse lobe component, for which the magnitude is distributed evenly for all the viewing directions. The radiance of the surface in the sensor direction may be expressed as the sum of all three components, as shown in Equation 2.1:

$$L = L_{diffusion} + L_{specular-lobe} + L_{specular-spike} \tag{2.1}$$

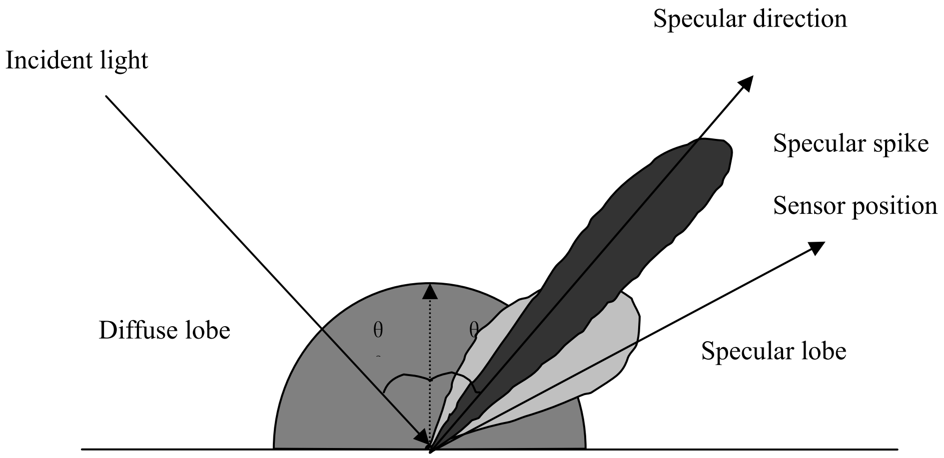

Figure 2.1 Nayar's unified surface reflectance model

2.2 Specular surface inspection methods

In the problem of inspection on uniformly colored specular surfaces, most past research falls into two major categories, based on the measured signals:

1. Intensity pattern inspection: specular highlight reflection [14], diffuse reflection, double-pass retroreflection [15], and grid reflection [16]
2. Phase shifting inspection: fringe projection [17] and phase reflection

Phase shifting inspection technologies measure the spatial phase shifting on the three-dimensional range images from a projected fringe pattern. They not only yield qualitative measurements, but also a three-dimensional quantitative measurement on the surface faults as small as a micrometer in depth. However, compared with the intensity pattern inspection technologies, phase shifting evaluations are highly computationally intensive, especially in cases where a huge amount of the surface image data has been generated and must be analyzed and classified in a short period of time, which is a common requirement for some industrial inspection applications. Among those intensity-pattern inspection technologies, double-pass retroreflection provides high sensitivity only on a highly specular surface that is provided by the application of a thin uniform fluid film. Similarly, a grid reflection technology is also only applied on highly specular surfaces because it treats the surface under inspection as a mirror. In contrast, specular highlight reflection inspects the surface curvature variation by observing the reflected specular light and can provide the necessary sensitivity. Diffuse illumination eliminates shadows, greatly reduces the effect of the specular reflections and yields images with optimal image intensity contrast for the later surface defect detection. So a combination of specular image and diffuse image information provides both the necessary sensitivity and the ability to measure quantitatively on the specular surfaces.

2.3 Existing on-line paint quality inspection systems

ABIS (Automatical Body Inspection System) [19] is a car body inspection system to automatically check the car-bodies on the production line for dents and ripples. Two components are integrated into the production: a sensor portal with range sensors that scan the whole surface of the body and a portal with robots that mark regions with detected defects. The processing chain can identify the car type, acquire data, as well as detect, analyze, and classify defects automatically. But it is only designed to detect defects on unreflective surfaces like unpainted sheet metals or plastic panels.

The Diffracto system is commercialized with the trademark *D-Sight*. The D-Sight optical set-up consists of a light source, a camera, a retroreflective screen, and the specimen. An optical double-pass retroreflection surface inspection technique developed by Diffracto Ltd in Canada [20], it is a real-time technique for visualizing small out-of-plane surface distortions and is particularly applicable to the rapid and enhanced visual inspection of large surfaces. However, the D-Sight method only operates if the surface of the object to be inspected is specularly reflective at high levels. Also, the contrast in the D-Sight signature of surface defects is strongly reduced as a result of ambient environmental light. Shielding is therefore necessary when a D-Sight inspection system is to be used in the field. Moreover, when inspecting curved surfaces, the D-Sight equipment should be orientated in such a way that the direction of curvature is perpendicular to the direction of observation of the D-Sight equipment. So the curvature of the target surface must be determined before the detection process can be performed.

AutoSpect [36, 37] is another commercial on-line painting quality inspection system developed by Perceptron Inc. The system consists of an inspection arch, sensors, a control panel, and a paint process monitor. It is a non-contact, automated measurement system that checks the critical characteristics affecting the appearance quality of painted surfaces such as orange peel and distinctness of image and gloss. However, according to reports, the reliability and consistency of inspection results still need to be significantly improved.

Over all, existing on-line paint quality inspection systems are currently insufficient to provide robust sensing of tile surface quality (or related surfaces). for the following reasons:. Some of these systems, such as ABIS, are very costly. Second, all of tlyhem focus only on a certain narrow aspect of paint appearance. Therefore, in this study, where the objective is to develop a robust, low-cost real-time system to assess the surface quality of ceramic tiles, Nayar's reflectance model will be used. Although the testbed sample in this work is ceramic tiles, it is expected that the resulting design will be effective for a class of relatively smooth specular surfaces.

CHAPTER 3

PAINT SURFACE DEFECTS AND THEIR MATHEMATICAL MODELING

This Chapter presents suggested models to characterize common defects in smooth specular surfaces, based upon the reflectance model that was introduced as an appropriate rational basis in Chapter 2. The chosen testbed for this investigation is ceramic tile surface defect inspection. So in Section 3.1, common paint defects on the surface of ceramic tiles are investigated and identified. In order to qualitatively analyze the surface specular reflection around the defect area, a standard Gaussian curve is shown to model one common defect, the seed defect, with the support function representation described in Section 3.2.. Furthermore, defect inspection mechanisms based upon specular reflectance information are explained in section 3.3.

3.1 Paint surface defects

There are several factors that cause the appearance of flaws in the process of painting ceramic tiles. A main physical cause of paint defects is the variation of surface tension forces along the film surface while painting and drying. Other causes include environmental and human factors, such as airborne particles like dust and dirt being trapped in the paint coating while drying. Also, liquid drops such as oils and silicon from the plant environment can penetrate the freshly painted surface to cause defects. According to a DU PONT report [21], there are fourteen types of typical paint defects in the booth area that affect the quality of surface appearance. The defects detected in this work are seed defects and spot defects. Their geometries have dimensions ranging from approximately a millimeter to several centimeters in height and lateral extent; smaller defects are not consistently discernable by professional human inspectors. Seeds can be characterized as raised bumps with a discernable height which are present on paint surfaces. They can be caused by the thinness of the color coat; improper filtration, which may results in contaminents trapped in the coating; out of spec raw materials or the incorrect reducing solvent during the painting process. Spots are planar: spot-like, or linear faults such as scratches. They have little geometric variation, but a relatively intense contrast to the non-defective surrounding surface.

Both defects affect the customers' purchase decision negatively. Depending on the specific industrial application and product category, their effects on the surface quality evaluation may be different.

3.2 Seed defect mathematical modeling and support function representation

As discussed in Section 3.1, seed defects in ceramic tiles are caused by myriad factors. Their shapes are irregular and their sizes are various, ranging from millimeters to centimeters. So it is challenging to find a single mathematical model that can accurately and completely describe the shapes of all seed defects. However, a reasonably simplified mathematical model can still aid in characterizing a defect's geometric properties by facilitating an understanding and qualitative analysis of the surface specular reflection around the defect areas; such a model can also aid in determining the defect inspection mechanism.

In this work, the standard Gaussian curve is proposed to model regular seed defects. The two-dimensional standard Gaussian function has the mathematical representation of

$$\Phi(x) = \frac{1}{\sqrt{2\pi\sigma}} \exp(-\frac{x^2}{2\sigma^2}) \tag{3.1}$$

Figure 3.1 illustrates the effect of the parameter σ in Equation 3.1; the Gaussian curves in this figure emulate typical real-world variations in seed defect profiles. Figure 3.2 further illustrates this by comparing a three-dimensional Gaussian model with simulated images of seed defects; the simulated images contain 3-D examples of the seed defect profiles modeled in two dimensions in Figure 3.1.

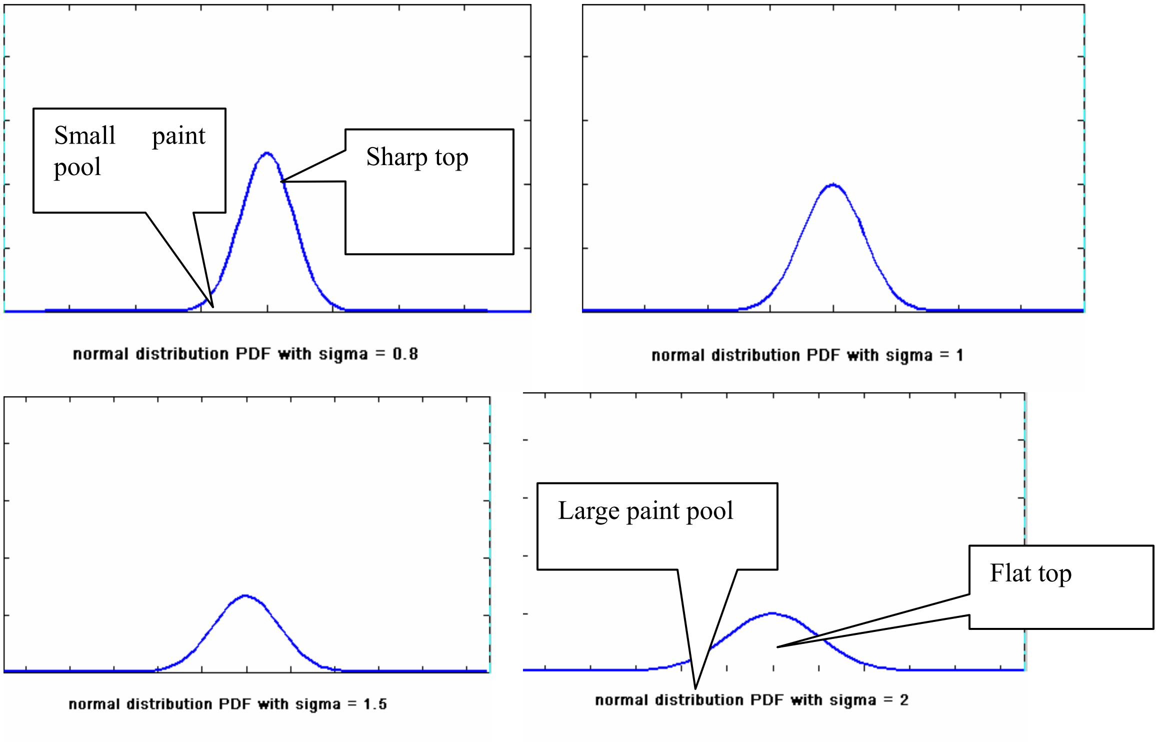

Figure 3.1 A group of 2-D Gaussian models of seed defects

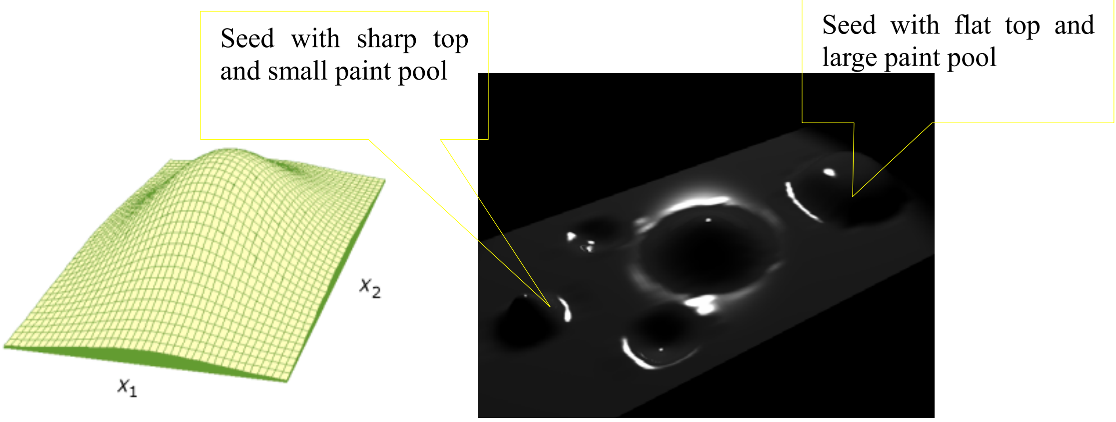

Figure 3.2 A comparison between 3-D Gaussian model and a simulated image of seed defects

The Gaussian curve representation of equation 3.1 successfully models some regular shapes of seed defects in the Cartesian coordinates. However, this mathematical representation results in undesired complications when describing the geometry of specular reflection. The reason for such complications is that specular reflection depends not only on the spatial coordinates of the surface reflectance profile, but also on its local surface normal.

To overcome such disadvantages, the proposed Gaussian curve function can be transformed into a representation based on the support function of a curve [22]. The support function representation of a curve has the form

$$\begin{cases} \theta_n = \tan^{-1}(-\frac{1}{y'(x)}) \\ \rho_n = x\cos\theta_n + y\sin\theta_n \end{cases} \tag{3.2}$$

θ, ρ and the support function representation are shown in a Cartesian coordinate system in Figure 3.3. Equation 3.2 can be also transformed into a more efficient state-space support function representation:

$$\begin{pmatrix} \rho_n \\ \rho_n' \end{pmatrix} = \begin{pmatrix} \cos\theta_n & \sin\theta_n \\ -\sin\theta_n & \cos\theta_n \end{pmatrix} \begin{pmatrix} x \\ y \end{pmatrix} \tag{3.3}$$

$$\begin{pmatrix} x \\ y \end{pmatrix} = \begin{pmatrix} \cos\theta_n & -\sin\theta_n \\ \sin\theta_n & \cos\theta_n \end{pmatrix} \begin{pmatrix} \rho_n \\ \rho_n' \end{pmatrix} \tag{3.4}$$

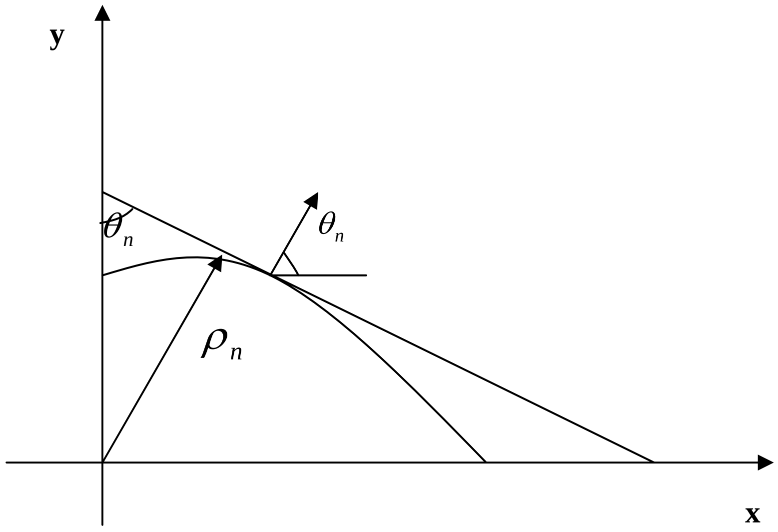

Figure 3.3 Representation of the support function of a curve

This second support function representation has the advantage of depending explicitly on the slope of the curve so that, under a rotation of the coordinate system, ρ_n remains unchanged and θ_n is only subjected to a simple linear shift.

3.3 Specular reflection on the surface with seed defects

The importance of specular reflectance information has been broadly recognized by researchers studying paint appearance over the years [23] [24]. A perfectly specular surface is defined as a surface that reflects a light ray in a single direction from any given point reflected on it, where the angle of the reflected ray with respect to the surface normal at the point is equal to the angle between the normal and the incident ray. The normal, incident, and reflected rays lie in the same plane. Specular reflectance models are widely used to describe mirror-like reflections from specular surfaces like glass, ceramic, polished metal, and some plastics; the reflected illumination from these real-world materials is concentrated in the specular direction. So for a defect free highly specular flat surface, a camera at an off-specular angle will capture essentially no light energy. This is illustrated in figure 3.4 where the camera angle β is significantly greater than the incident angle

α .

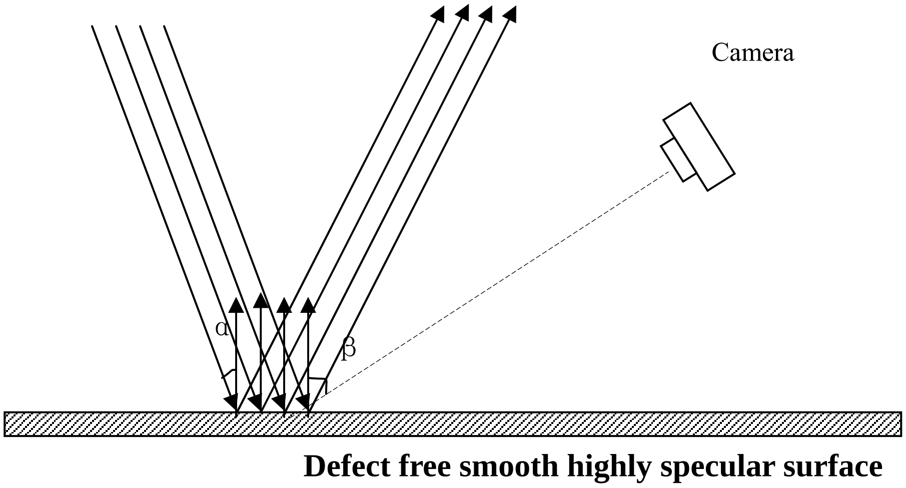

Figure 3.4 Specular reflections on a defect free surface

However, when any geometric imperfection exists, such as a seed defect present on the inspected surface, those incident rays that hit the seed surface will yield local specular reflection rays whose directions are significantly different from those produced by the background surface, as illustrated in Figure 3.5. Figure 3.6 shows more details for the surface specular reflections around the defect area. Because the curve of the seed defect surface is continuous, the resulting specular reflections will be distributed in a large range of angles as shown. In this situation, the camera, placed at a fixed off-specular angle, will capture some of those irregular reflections due to the presence of defects.

A camera consists of an image plane and a lens, as presented in Figure 3.7 and provides a transformation between the object space and the image space shown in Figure 3.8. Thus, captured reflection light rays from a seed defect will be transformed into a group of high intensity pixels on the image plane; this group may be considered as a highlight blob. Here, a blob is defined as a group of connected pixels with similar intensity values. The presence of highlight blobs on the image captured by the camera at an off-specular angle indicates the presence of surface imperfections for an otherwise flat surface. The shapes and locations of the image blobs are closely related to the shapes and physical locations of the real defects.

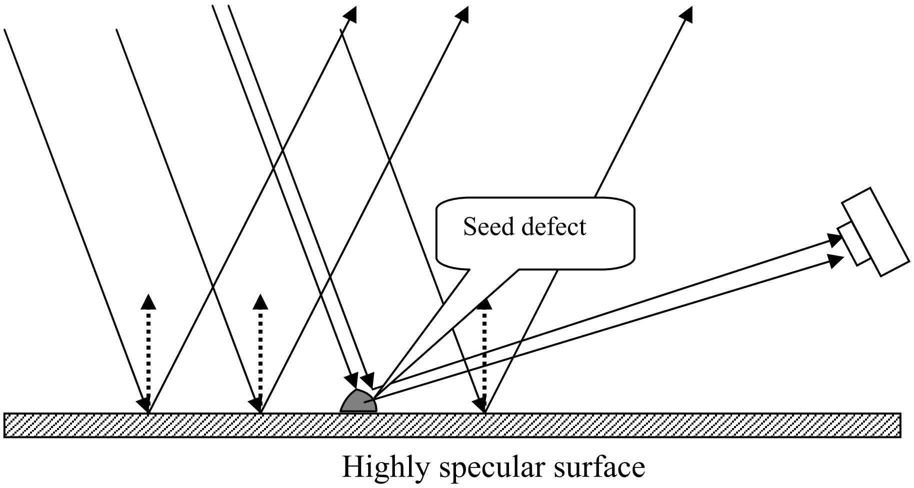

Figure 3.5 Specular reflections on a surface with seed defect

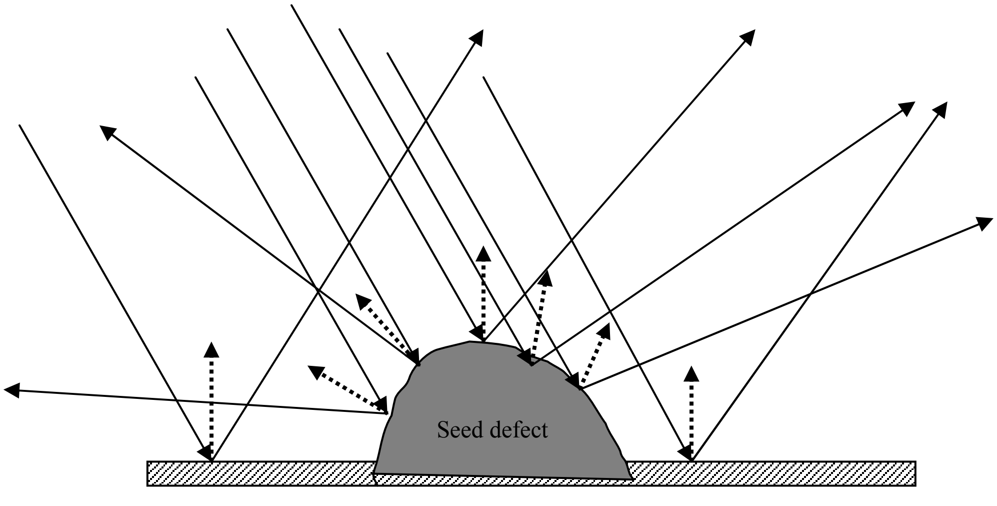

Figure 3.6 Specular reflections around the defect area

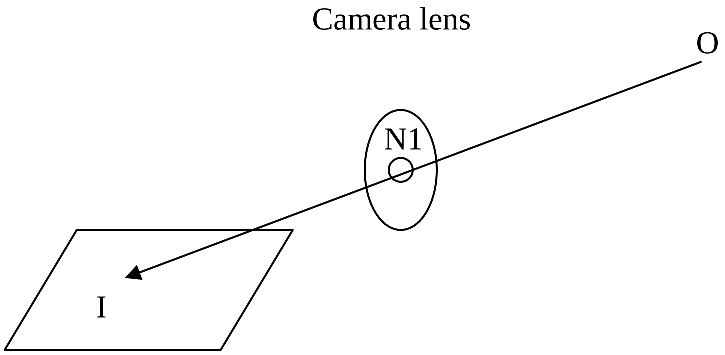

Figure 3.7 A Basic camera model

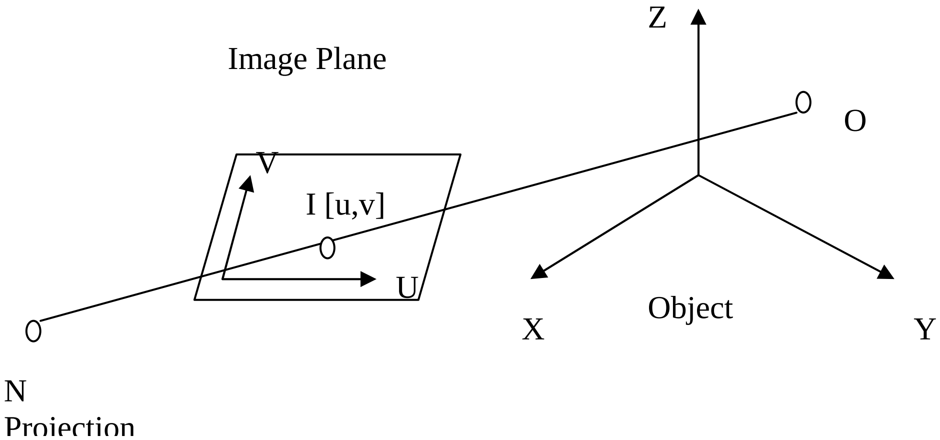

Figure 3.8 A geometric camera model

CHAPTER 4

APPARATUS SELECTION AND EXPERIMENT TESTBED SETUP

Lighting and cameras are two important elements of any visual inspection system. To more accurately transfer information about the physical world, light acquired by the detectors, such as a camera, must provide sufficient contrast in order to distinguish the primary features of interest from others, including noise. This chapter discusses apparatus selections for the experiment testbed used in this study as well as the experiment testbed structure and its setup.

4.1 Experiment Source illumination

Two different light sources are selected in this experiment for different inspection purposes: an incandescent directional illumination system and a diffuse illumination system. Their detailed specifications and functions are discussed throughout the next few pages.

4.1.1 The incandescent illumination system

The incandescent directional illumination system is used for specular surface inspection at diffuse camera angles. A light source that emits visible light as a result of being heated is called an incandescent light source. In an incandescent light source, the colliding hot atoms emit photons that form the packets of light. Because of its steady light intensity output, easy light intensity control and low cost, the incandescent light source is the most commonly used light source in appearance measurement studies. Sunlight is the best example of an incandescent light source.

The incandescent illumination system used for this study is a Fostec DCR-II DC light source with a Fostec A08080 collimator and a Fostec A20650 light intensity controller. A collimator is a device capable of collimating radiation, and is a long narrow tube in which strongly absorbing or reflecting walls permit only radiation traveling parallel to the tube axis to traverse the entire length. The light is conducted through a fiber optic bundle. A collimating lens is then set at the end of the fiber bundle to implement the directional illumination. The variable-intensity light source is a 150-watt incandescent light source with a low voltage ripple that provides a stable light intensity output between 0 and 150 watts which can be held within 1%. Its intensity can be manually or digitally adjusted by the light intensity controller.

4.1.2 The LED diffuse dome illumination system

Another selected light source for this study is an LED diffuse dome light source. The diffuse dome light illumination provides intense uniform light for inspecting objects with highly reflective, specular, round or uneven surfaces. The diffuse dome light has a high level of diffuse illumination that eliminates shadows and greatly reduces the effect of the specular reflections. It also has a bigger illumination area compared with other light sources with similar functions, i.e. linear fluorescent illumination. Moreover, compared with a regular fluorescent light, LED illumination is more energy efficient, longer lasting and provides a consistent output.

The diffuse illumination in this experiment testbed consists of the model DL7248, a diffuse dome light source with white light, and a separate Advanced Illumination CS300-IC constant current source with intensity control from the Advanced Illumination Inc, as shown in figure 4.1. Its LED standard product lifetime can be 100,000 working hours with a projected light distribution less than 5% over the illuminated area. The current source can supply 30 watts output to provide the light source safe, consistent, optimized power levels with controllable intensity. The light is reflected off the interior of the dome, resulting in 360-degree diffuse and even illumination that is illustrated in figure 4.2.

Figure 4.1 Model DL7248 diffuse dome light source

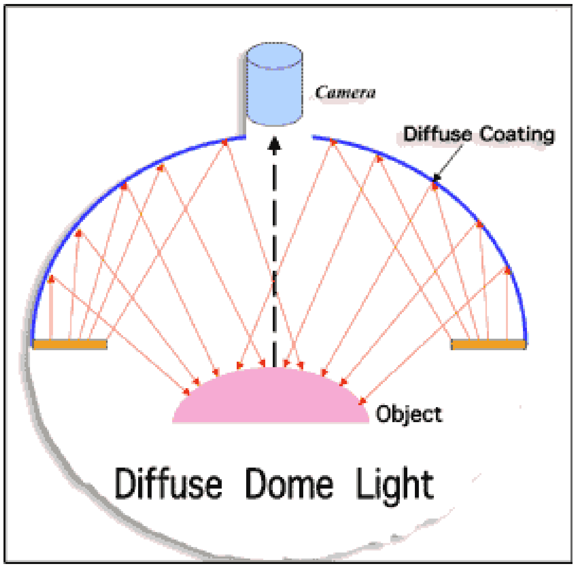

Figure 4.2 Diffuse dome light source illumination model

4.2 SmartImage intelligent sensor

The camera used in the experiment testbed is the DVT Series 530 SmartImage sensor [33]. It consists of hardware that includes a digital camera with strobe illumination and an isolated breakout board, and software that includes the Framework graphic user interface. It is a self-contained intelligent machine vision system with on-board image acquisition, processing, digital I/O, and serial and Ethernet communications. It does not require a separate processor or frame grabber. All these functions are contained within its own small board. The camera has its own built-in central processing unit with registers and flash memory. So it can execute simultaneous image samples and analysis. The isolated breakout board not only provides a convenient method to connect digital I/O, power and strobe illumination lines; it also allows for the use of isolation modules. More details about this sensor are given in Appendix A.

4.3 Experiment testbed setup and inspection flowchart

The experiment testbed structure is schematically presented in figure 4.3. The system is integrated from three independent functional blocks, marked with A, B, and C respectively. Through a transportation belt, a ceramic tile is first inspected in block A by using a collimated incandescent light source, and the sensor is set at a large off-specular angle to capture the specular reflections due to the presence of defects. After the specular inspection process, the tile is transported to block B for diffuse inspection. The system inspects the surface planar faults such as spots under the diffuse dome light illumination. Meanwhile, selected images and data are transferred to a connected local computer terminal in block C for further processing and classification, if necessary. Details about each functional block are given below.

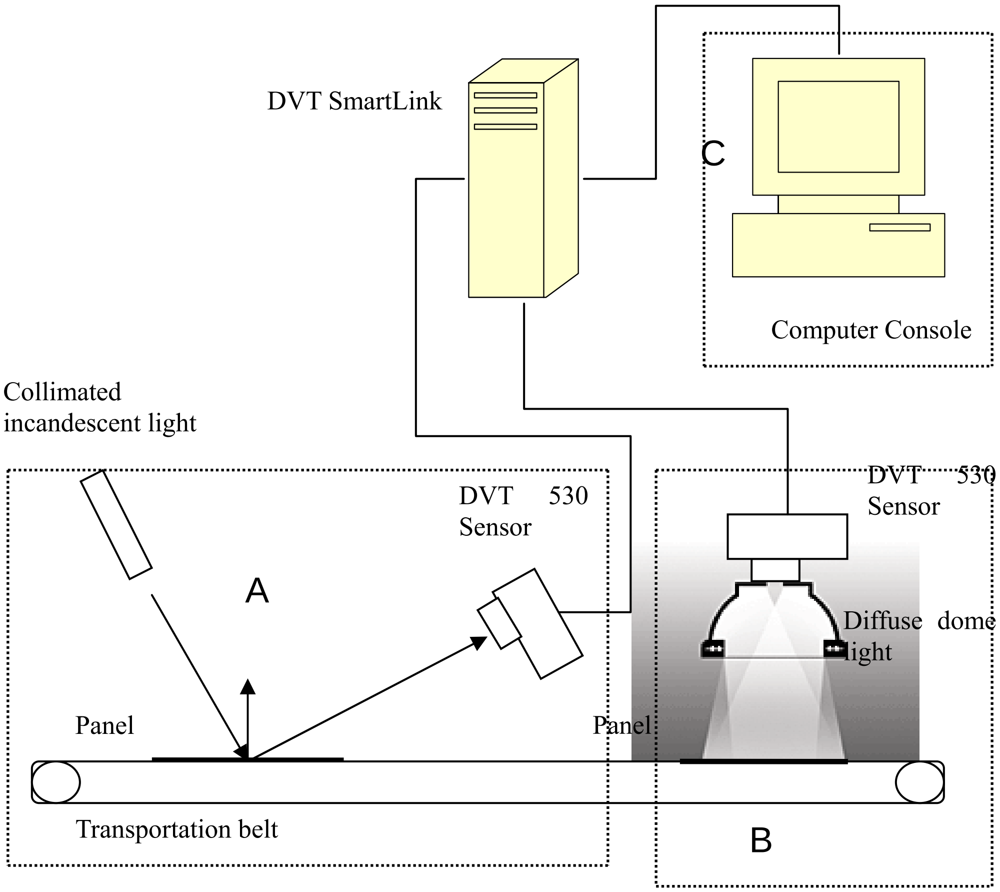

Figure 4.3 Experiment testbed

- <u>Block A: Specular inspection</u>

This stage consists of a collimated incandescent light source and a DVT 530 series SmartImage sensor. An optimum geometric setup has a fixed illumination angle, α, of 30 degrees and a fixed sensor angle, β, of 65 degrees. A top view of the experimental platform and its two dimensional schematic is illustrated in figure 4.4.

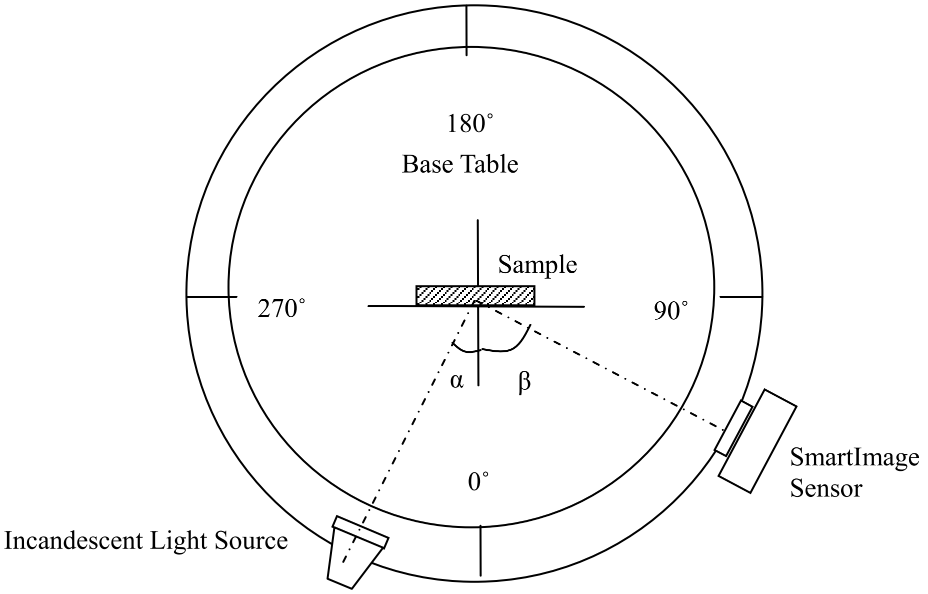

Figure 4.4 Experimental testbed - part A - two-dimensional schematic plot

- <u>Block B: Diffuse inspection</u>

The components in block B consist of a diffuse dome light source and a DVT 530 series SmartImage sensor. The diffuse dome light source is positioned 70 mm directly above the sample surface. Figure 4.5 shows two-dimensional side-view schematic.

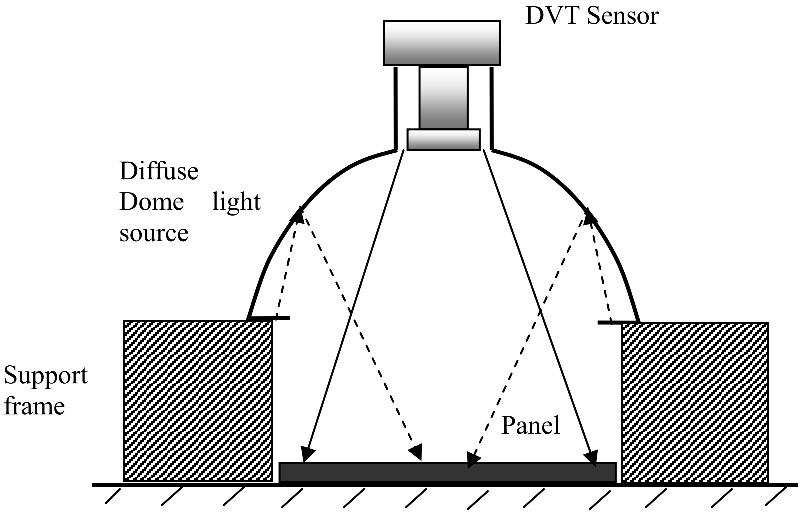

Figure 4.5 Experimental testbed - part B - two-dimensional schematic plot

- Block C: Computer terminal for advanced image processing

A computer collects, displays and analyzes images and data from both SmartImage sensors though the DVT SmartLink. The computer is a Dell Dimension 4500 series desktop computer with Intel Pentium 4 processor at 1.8 GHz and 256 MB memory.

Because each sensor functions as an independent machine vision system with image capturing, processing and communicating functions, compared with the traditional modular approaches, the designed system architecture described here significantly simplifies the inspection synchronization process between different sensors and with other terminals (e.g., a PC). Multi-camera image capture can be synchronized through simple SmartLink hardware. This significantly increases the system inspection rate by saving the image data transfer time and reduces the cost as well.

Moreover, figure 4.6 gives the system inspection flowchart. Figure 4.7 further illustrates this inspection process in pseudo computer language.

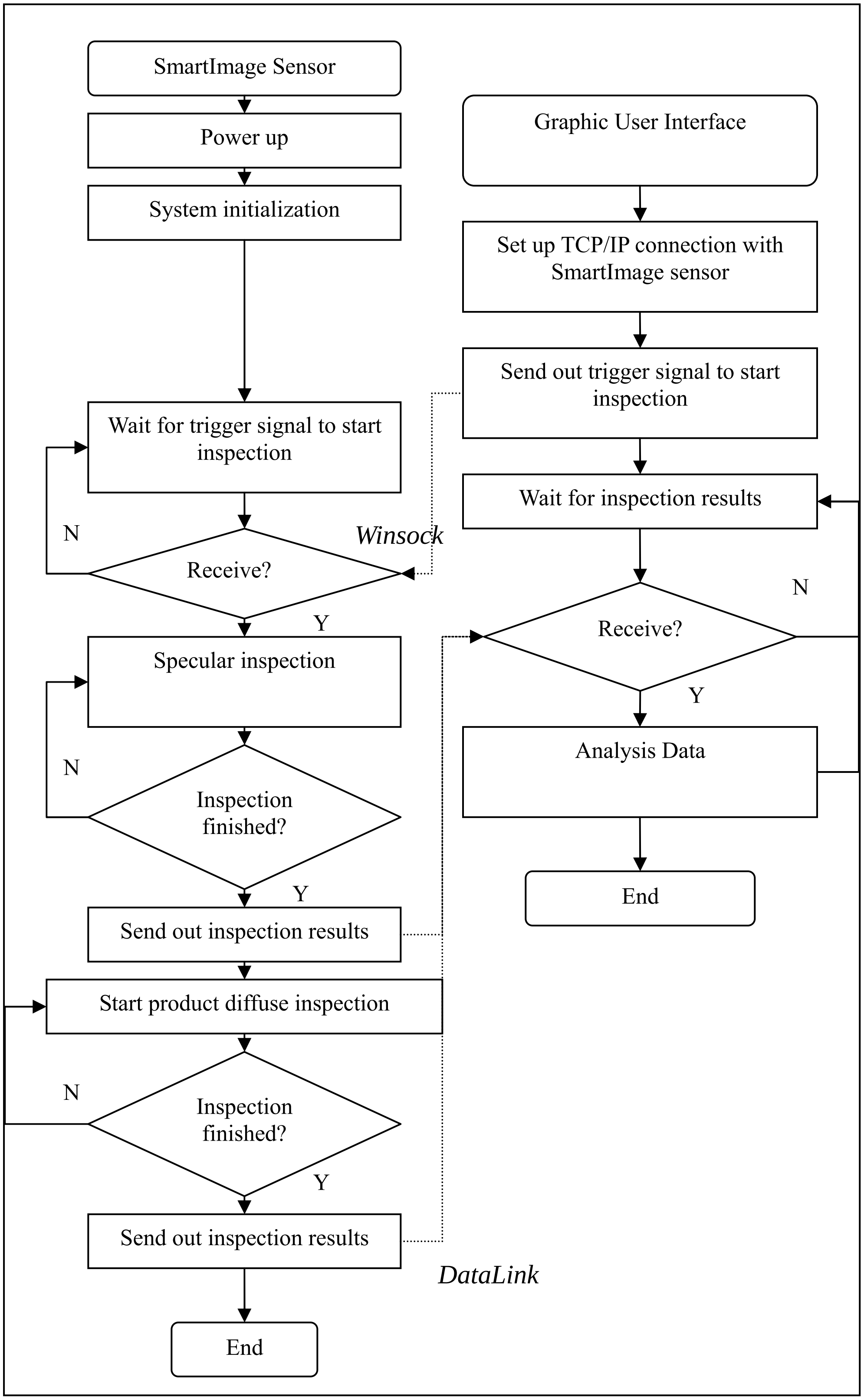

Figure 4.6 Experiment Inspection system flowchart

```
class Defect Inspection
{ public static void main()
{
// Initialization
// Restore Product ID from DVT sensor flash memory
Flash F = new Flash();
F.RestoreRegs();
Product P1, P2
// P1, P2 define specular inspection and diffuse inspection
P1 = GetProductById(RegisterReadByte(4010));
P2 = GetProductById(RegisterReadByte(4020));

// Variable to monitor success of operations
int res = 0;
// Variable to monitor desired outputs
long Bit = 1;
int inBit = 1;
// Starting loop to execute indefinitely
while (true)
{
// Wait for input 24 as a trigger signal to start inspection
res = WaitOnInput (24,-1);
if (res == 0)
```

Figure 4.7 Pseudo background script language for the inspection flowchart

```
{
// Wait for input 24 as a trigger signal to start inspection
res = WaitOnInput (24,-1);
if (res == 0)
{
P1.Select(); // Set product P1 as active inspection product
Inspect(); // Start product P1 inspection
// Wait for the inspection results by monitoring the busy output
while ((GetOutPuts() & (Bit << 3)) != 0);
// Send out inspection results via DateLink
// Select another product and trigger the inspection
sleep (250); // Pause execution for 250 msec
P2.Select();
Inspect();
while ((GetOutPuts() & (Bit << 3)) != 0);
// Wait until input is low again
WaitOnAnyInput (0,inBit << 24,-1);
}
}
}
```

CHAPTER 5

DEFECT DETECTION AND FEATURE EXTRACTION

Knowledge of the reflectance properties of specular surfaces (as described in Chapter 3) is used to analyze seed defects which yield highlight blobs on a diffuse-angle image under the directional incandescent illumination conditions discussed in Chapter Four. Also, the defect plane contours are captured as dark or white blobs on the diffuse image under the diffuse illumination, as also discussed in Chapter Four. Image processing algorithms are proposed in this chapter to accurately detect such individual dark and white blobs and extract their shape features from both the specular images and the diffuse images.

5.1 Defect detection

1. Dark blob detection - intensity based Auto Bimodal threshold: An intensity based Auto Bimodal threshold detects the dark blobs on the image. It automatically calculates a single threshold value to use based on the entire image histogram (figure 5.1). Since it uses all the pixel values in the area to calculate the threshold, the effects of noise and specular reflections are minimized. The threshold is recalculated for each image.

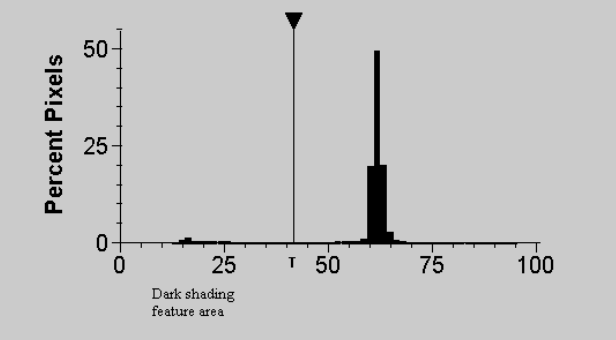

Figure 5.1 Histogram of a specular surface image with defects

(T is Auto Bimodal threshold value)

2. Light blob detection - gradient based edge detection: A Gaussian filter smoothes the image. Then the canny edge detector performs quick and simple edge detection.

The canny edge detector [25] detects the edge feature of the individual defect. Edges in the image are curves where rapid changes occur in intensity or in the spatial derivatives of intensity. In this investigation, edges will generally be caused by the surface imperfection in that area. Edge detecting in an image then significantly reduces the amount of data and filters out useless information, while preserving the important structural properties of the defects that are used for later feature extraction.

Generally, Canny edge detectors follow three criteria for optimal edge detection:

(1) Good detection ability, that is, there should be low probabilities of failing to detect real edges and falsely detecting edges that do not exist

(2) Good localization ability, that is, the position of the detected edge should be as close as possible to the true position of the edge

(3) Uniqueness of detection, that is, a given edge should be detected only once.

There are three parameters in the Canny edge detection algorithm:

1. Sigma: this parameter is used to select the Gaussian filter. The Gaussian filter is used to filter out any noise in the original images before trying to locate and detect any edges. The larger the width of the Gaussian mask, the lower is the detector's sensitivity to the noise. The range for this parameter in this experiment is from 0.40 to 2.40.

2. tlow, thigh: they are used to eliminate the streaking in the hysteresis. Streaking is the breaking up of an edge contour caused by the operator output fluctuating above and below the threshold. For this experiment, parameter tlow is selected between 0.40 and 0.80 and parameter thigh is from 0. 80 to 0.99.

The processing steps are:

1. Convolve the image with a separable Gaussian filter.
2. Take the first derivatives of dx and dy by using [-1, 0, 1] and [1, 0, -1]’.
3. Compute the magnitude: sqrt (dx*dx+dy+dy).
4. Perform non-maximal suppression to assign edges
5. Perform hysteresis thresholding

Once all the edges of the defects in the image have been retrieved by the Canny edge detector, the contour can be extracted by the image structure analysis algorithm such as the Run Length Encoding of chain codes, higher order Freeman codes, polygonal approximation, etc. The Rosenfeld-Johnston algorithm [26] is one of the earliest algorithms to determine the dominant points on the digital curves. The basic concept of the algorithm is to calculate the curvature of each point in the line, and then the points with the local maximum in curvature are designated as dominant points. However, the difficulty for this algorithm lies in the selection of the neighborhood radius parameter and its identity for all the points. Teh and Chin [27] introduce a parameter free algorithm. It is based on the use of the maximum and minimum curvature points to vectorize. However, the results appear to be sensitive to quantization and boundary noise. The Douglas-Peucker Approximation is used in this study to find the contour on the edge images. The idea is to apply some simple approximation techniques to the chain code with polylines, such as substituting ending points for horizontal, vertical, and diagonal segments, and then using the approximation algorithm on polylines. This preprocessing reduces the amount of data without any accuracy loss.

After getting the defect contours on the image, the next task is to fit primitive models to the image data. The method used in this study is ellipse fitting [28] for the defects with near circular or elliptic planar contour and line fitting [29] for the linear defects such as scratches. Both models greatly reduce and simplify the data and also give an approximate description of those regular surface defects.

5.2 Defect feature extraction

For the defects with irregular planar edge contours, two simple shape descriptors, compactness and convexity, are proposed for characterization [30].

Compactness measures the "roundness" of the feature object and can also yield information on surface roughness. Relative compactness is defined as the ratio of the perimeter of a circle with the same area as the original feature object and the original perimeter. Here P and A represent the perimeter and the area of the feature object respectively, as derived from the image.

$$comp = \frac{P_{circle}}{P} = \frac{2\sqrt{\pi A}}{P} \tag{5.1}$$

Convexity measures the regularity of the feature object's contour. It is defined as the ratio of the perimeter of the convex hull and the original perimeter. The convex hull is the minimum convex covering of the object.

$$conv = \frac{P_{convexhull}}{P} \tag{5.2}$$

Internal structure measures the distribution of gray levels in a featured object (defect). The average intensity of each defect feature in the original image is measured with the following equation.

$$avg = \frac{\sum_{i=1}^{N} I_i}{N} \tag{5.3}$$

CHAPTER 6

INSPECTION IMPLEMENTATION

This chapter discusses details of the experimental implementation. Based on the discussion of the experimental setup in Chapter Four, every ceramic tile undergoes two consecutive inspections: first, a diffuse angle inspection and then a diffuse illumination inspection, in order for its surface quality evaluation to be completed. Different algorithms from chapter five are used to analyze and process the captured image at each stage. Here the term "Product" is used to define such a specific inspection task in the SmartImage sensor system. The diffuse angle inspection task is named Product *HighlightGrabber* and the diffuse illumination inspection task is named Product *DiffuseCatcher*. Also, “a complete inspection” is defined as a series of consecutive inspection processes starting from image sampling, image analysis to finally result in the display and output. So, every single ceramic tile takes two complete inspections, first the Product *HighlightGrabber* and second the Product *DiffuseCatcher*. Moreover, a third Product *AutoCalibration* is used for the camera calibration. Calibration results such as camera focal length, translation vector, rotation matrix and distortion coefficient etc. are stored into the SmartImage sensor ROM so that they can be directly referred to by other inspection products during the inspection in order to transform the desired feature coordinates such as defect locations from the image space into the real world space. And Product *AutoCalibration* is only active when the testbed setup, i.e. the camera position, changes, in which case the system needs to be recalibrated.

6.1 Camera calibration

The camera is calibrated in order to transform the center positions and the area of defects from a camera image space into real world coordinates. Here the SmartImage sensor’s built-in calibration function is used to calibrate the camera system so that other products can directly refer to the results during the inspection.

The process of camera calibration in the Framework is:

1. Print a black and white checkboard pattern and paste it on a test panel
2. Place the panel on the testbed
3. Use Intensity Softsensors to extract the square centers of the check board image
4. Create a Coordinate System Softsensor with the parameter "global calibration" checked and use the output from the Intensity Softsensors from step 3 as the input calibration points
5. Run the calibration program
6. Store the calibration results into the SmartImage sensor ROM

6.2 Diffuse Angle inspection

The diffuse angle image is captured by the camera at an off-specular diffuse angle under the incandescent light illumination. Reflectance, which is caused by the presence of defects, is captured as the highlight blobs on the image (figure 6.1). The dynamic intensity based threshold method is used to extract those highlight blobs from the image. This dynamic threshold places the threshold at some location between the minimum and maximum intensity values, based on the value set by the user. The intensity-based dynamic threshold level I is determined by the user-defined parameter T, and is

$$I = (I_{\max} - I_{\min}) \times T + I_{\min} \tag{6.1}$$

For this experiment, parameter T is 30%.

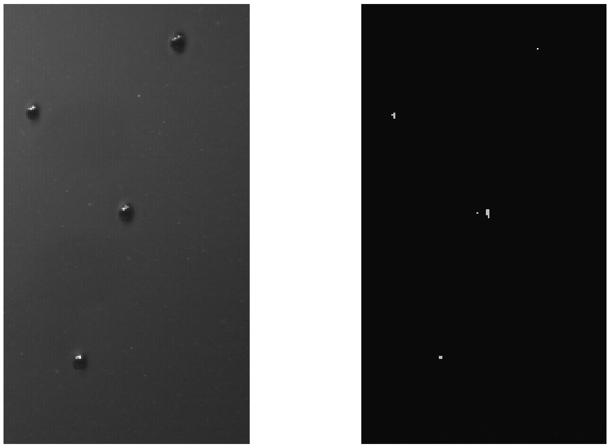

Original specular image Highlight image after thresholding

Figure 6.1 Images from a specular inspection

6.3 Diffuse Illumination inspection

A diffuse illumination image is captured by the camera right above the inspected product under the diffuse illumination. Multi-grade image-processing algorithms are proposed to detect and extract both dark and white defect blobs on the diffuse images in order to discern and characterize many different kinds of defects. Here, to increase the inspection precision while still being robust with respect to the noise on different images, the Gaussian mask parameter of the edge detector is combined with a minimum defect feature size threshold. Each image is processed by three different approaches: one is Auto Bimodal; the other two are edge detectors using differently sized Gaussian masks. That is, a small Gaussian mask with a small minimum-size threshold cap is used to detect regular light blobs such as spots. A wider Gaussian mask with a large minimum size threshold is used to detect those defects with a lower image intensity contrast such as scratches. Parameters are pre-set for each batch of test samples with different coatings based on the rule from [29].

The defect features are then extracted and their shape information, such as their center location, area, compactness, and convexity are calculated. As an example, Figure 6.2

shows a group of inspection images captured for one test panel. Table 6.1 lists the corresponding system output.

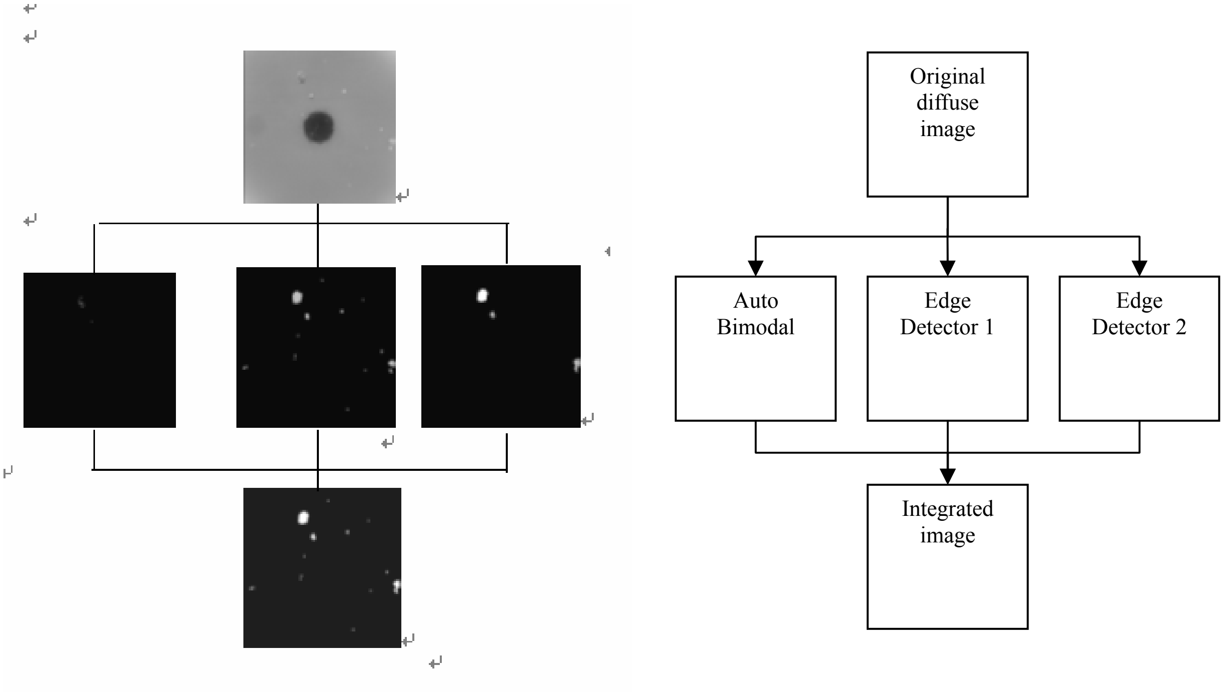

Figure 6.2 Diffuse image inspection

Table 6.1 Output from a diffuse inspection

Defect index	Center x position (mm)	Center y position (mm)	Area (pixel)	Comp	Convex	Avg. intensity
1	83.8	108.3	12	0.874	0.712	67.23
2	73.6	101.2	569	0.813	0.551	70.02
3	100.8	100.2	11	0.621	0.714	51.38
4	92.0	95.4	40	0.449	0.211	52.44
5	77.8	93.5	121	0.580	0.654	61.18
6	74.0	85.5	15	0.901	0.342	53.24
7	108.8	79.1	26	0.372	0.401	55.48
8	72.8	77.0	24	0.662	0.613	60.21
9	113.1	73.3	287	0.884	0.811	49.07
10	52.2	72.4	41	0.815	0.372	58.27
11	112.7	71.0	45	0.712	0.563	56.08
12	102.0	71.3	14	0.842	0.752	37.29
13	94.6	55.3	15	0.915	0.834	60.35

CHAPTER 7

RESULTS AND DISCUSSION

This chapter presents the results from the inspection system output on the real ceramic tiles. Also, the system inspection time is measured to illustrate that the designed system meets the ceramic tile real-time inspection requirement.

7.1 Camera calibration verification

The objective of this section is to verify the accuracy of the calibration method and give the absolute error between the calibrated and measured results. First, table 7.1 shows the initial calibration verification results with test points randomly chosen from the central points of a standard black and white checkboard. From this table, calibration errors are less than 0.3 mm in the x direction and less than 0.2 mm in the y direction for a field of view of 152.4 millimeter by 152.4 millimeter.

Table 7.1 Calibration verification results I

Feature index	Measured x position (mm)	Measured y position (mm)	Calibrated x position (mm)	Calibrated y position (mm)	Absolute error in x (mm)	Absolute error in y (mm)
1	91.9	76.2	92.2	76.0	0.3	0.2
2	44.8	107.6	44.6	107.8	0.2	0.2
3	60.5	60.5	60.4	60.3	0.1	0.2
4	44.8	76.2	44.5	76.1	0.3	0.1
avg					0.23	0.18

Then in Table 7.2, the calibration method is further verified on a real ceramic tile from Figure 7.1. The center locations of seven seed defects on this panel are selected as the test points. The real positions are measured by a high precision digital ruler. The results are shown in table 7.2. The average calibration error is below 1 mm in both x and y directions; given the measurement uncertainty present and accuracy necessary, these position error results are reasonable and acceptable.

Table 7.2 Calibration verification results II

Index	Measure x position (mm)	Measure y position (mm)	Calibrate x position (mm)	Calibrate y position (mm)	Absolute error in x (mm)	Absolute error in y (mm)
1	66.0	106.1	65.9	106.6	0.1	0.5
2	101.6	106.0	101.9	106.6	0.3	0.6
3	89.8	83.9	90.0	83.9	0.2	0.0
4	46.1	69.2	45.4	69.4	0.7	0.2
5	113.7	57.8	114.2	57.3	0.5	0.5
6	71.9	57.1	71.3	56.9	0.6	0.2
7	98.5	44.7	98.8	43.6	0.3	1.1
avg					0.38	0.4.4

7.2 Inspect system output and discussion

The inspection system outputs both images and numbers that contain information such as the location, size, and shape of each individual defect. Together, that information is used for the product surface quality evaluation. It has been tested in the experiment system on more than fifty real ceramic tiles with different specular paint coatings. Some of them are defect free. Others may have defects, including spots and seeds with sizes in several to tens of millimeter scales. Inspection results from seven of them, panel A to panel G, are published in this thesis. Here, Figure7.1, Figure 7.2, and Table 7.3 show the experiment output of the test panel C. Test panel C is presented here because it is representative of a typical defective ceramic tile panel. Results for all other six panels are listed in Appendix C.

To calculate the detection rate, 20 test panels are randomly selected to compare the results from the inspection system output with the human inspection following the standard quality management. The detection rate for this system is 92.4%. And the false positive detection rate is 4.4%.

Table 7.3 Output from the diffuse inspection of test panel C

Defect index	Darkblob Area (pixel)	Bounding box Width (pixel)	Bounding box Height (pixel)	Conv.	Comp.	Peri. (pixel)	Whiteblob Area (pixel)
1	122	13	12	0.90	0.85	42	9
2	106	12	12	0.84	0.82	40	8
3	112	11	12	0.84	0.85	41	14
4	133	13	13	0.95	0.87	44	13
5	107	11	12	0.83	0.83	40	8
6	111	12	12	0.93	0.83	41	12
7	108	11	12	0.86	0.87	40	8
8	122	13	12	0.90	0.85	42	9

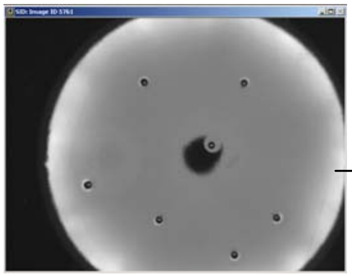

Original diffuse image of test panel C

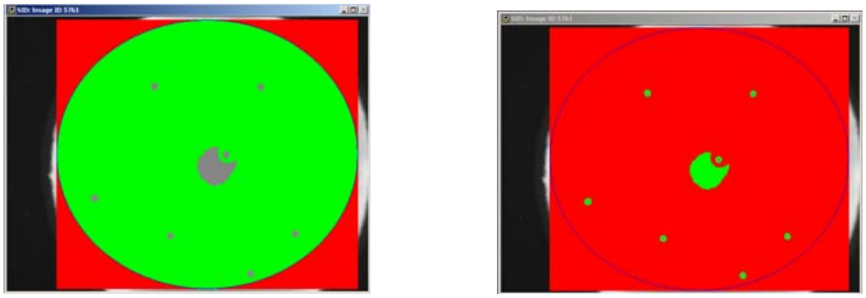

Image with marked dark features Image with marked white feature

(Before filtering and thresholding)

Image with marked dark features Image with marked white feature

(After filtering and thresholding)

Figure 7.1 Image from diffuse inspection of the test panel C

Figure 7.2 gives the specular image with the highlights of test panel C. Generally speaking, each highlight corresponds to a physical defect. However, from the experiment, there is the possibility that two highlights map to the same seed defect, which may be caused by the paint pool of the seed or the mirror reflection of the real highlights. The group of two highlights is defined as twin highlights.

If the presence of twin highlights is due to the paint pool, as shown in Figure 7.2, both highlights are generated by the real specular reflection over the defect surface. So their distance should be smaller than the size of the defect image contour. According to this calculation, to avoid detecting those two highlights as two different defects, the distance is calculated between each pair of highlights in this system. If they are lower than a preset limit, they are considered to be twin highlights.

Figure 7.3 shows another example of the twin highlights, which is caused by the mirror reflection of real highlights. It only happens on highly specular surfaces. Reference [31] gives a thorough investigation of this topic. The mirror highlight can be located out of the range of the defect image contour, depending on the shape of the defect. To reduce the error, the center position between the highlight and its mirror is calculated as the output position of the highlight in this case.

Instead of using the SmartImage sensor built-in calibration function for the camera calibration, as in the product *DiffuseCatcher*, here for the product *HighlightGrabber*, Tsai's camera calibration algorithm is used [32] in order to increase the calibration accuracy at a large camera angle. The detailed calibration is given in Appendix B. Table 7.4 gives the product *HighlightGrabber* specular inspection results of test panel C, which include the area and the real world position of the highlights. Moreover, the fourth column, the distance, in table 7.4 is calculated by the equation provided by 7.1. It compares the results of the defect physical location calibrated from Product *DiffuseCatcher* with the Product *HighlightGrabber*.

$$dist = \sqrt{(X_s - X_h)^2 - (Y_s - Y_h)^2} \qquad (7.1)$$

where (Xs,Ys) is the output of the defect physical center location from the inspection product *DiffuseCatcher*. (Xh,Yh) is the output of the physical center location of highlights of the same defect from the inspection product *HighlightGrabber*.

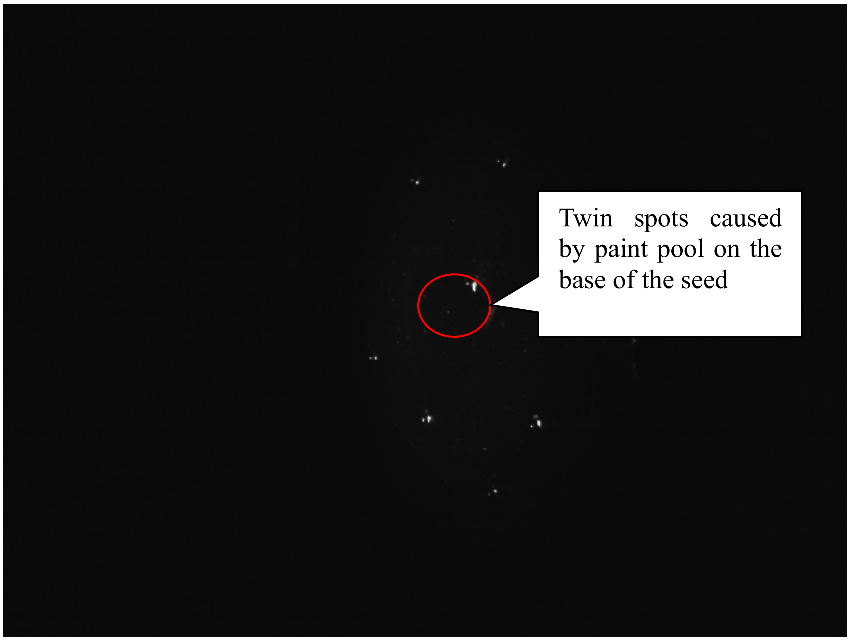

Figure 7.2 Image from specular inspection of the test panel C

Figure 7.3 Image from specular inspection with twin highlights

Table 7.4 Output from specular inspection of test panel C

	Image Area (pixel)	Highlight Position (mm)	Distance (mm)
1	1	(68.0,104.7)	2.8
2	1		2.7
3	12	(92.0,83.0)	2.2
4	1	(48.4,69.5)	3.0
5	6	(113.9,58.8)	0.5
6	6	(72.3,57.7)	1.3
7	1	(100.4,46.1)	3.0

Based on the experiment results, greater measurement errors in the highlight detection can be caused if:

(1) The highlight and its Mirror are regarded as two different seeds if their distance is larger than the preset limit, as in the Test panel F, G.
(2) The two seeds are so close to each other in the x direction that their highlights cannot be differentiated, as in the Test panel D.

The first error can be eliminated by increasing the preset limit. And for the second error, it makes sense to just consider those two seeds as one because their physical location is close.

7.3 System real-time inspection and timing

This results of this research will ultimately be used to design an on-line automated machine vision system for real-time defect inspection. So it is important to know how to measure and inspect time under this system's performance.

Real-time is defined as "of or relating to computer systems that update information at the same rate as they receive data, enabling them to direct or control a process such as an automatic pilot." (*The American Heritage® Dictionary of the English Language)* For this experiment, "real-time" only requires to guarantee a response to an external event within a given time. This time includes camera exposure time, image digitalization time, data-transferring time, image-processing time, and decision-making time. More specifically, the SmartImage sensor is used to acquire the test panel image and then process that data with the sensor built-in processor. Results are transferred to a connected computer to make the final surface quality evaluation. This last step is not necessary in an implemented on-line system; rather, it is used here to validate the appropriateness of the proposed rational basis.

In the next section, background knowledge and definitions related to the system inspection timing will be discussed and then an analysis of how to calculate or predict maximum system inspection rates will be performed. Not only because it will help us understand why this system is considered a real-time inspection system, but also it is critical for optimizing the system's inspection rate, avoiding resource conflictions and missed inspection, and synchronizing system inspection processes.

The SmartImage sensor system architecture is based on a CCD that is closely tied to a microprocessor. Images are exposed on the CCD, digitalized and then transferred directly to the microprocessor for analysis. During this process, image acquisition in the CCD and image processing in the microprocessor can occur simultaneously. Another important property is that the system executes single thread processing. The sampled image is stored in two buffers: the acquisition buffer, to store the acquired image, and the analysis buffer, to save the image under analysis. However, each buffer can only save one image at a time. So a new image cannot be acquired unless the last acquired image has been moved to the analysis buffer. Similarly, an image cannot be moved to the analysis buffer until the last image has been completely processed.

Based on the above knowledge, the inspection system timing is divided into three parts: image acquisition time, image processing time, and output processing time. Each of them can then be subdivided into various tasks, which are explained below.

The image acquisition time includes a delay after the trigger (this is a user-defined parameter to allow a fixed time delay after each inspection is triggered), an exposure time (another user-defined parameter) to yield acceptable image contrast, and a digitalization time, which is proportional to the size of the image being processed. A full image (640X480) digitalization takes about 40ms and can be reduced by partial acquisition.

The image processing time, also called Softsensor processing time, depends on the selected inspection products and their individual Softsensor parameters.

The output processing time is also named the data transferring time. It includes transferring the data through the sensor Data Link or processing the output based on user-defined settings. There is a simple equation to calculate the total time required to send the data through Data Link.

Total time = (# of char to be sent) * [(# of data bits) + (1 start bit) + (# of stop bits)]/ (transfer rate) (7.2)

All these parameters from equation 7.2 can be set and read from the Framework I/O parameters table.

Considering the sensor's single-thread processing technology, in general, the minimum time between system inspections or the minimum cycle time can be calculated with the following formula:

Maximum (delay after trigger + exposure time + digitalization time, image inspection time) (7.3)

Table 7.5 gives the time for a complete inspection of the three products in this system.

Table 7.5[1] Results of system product inspection time

Product	Max time for one complete inspection	Min time for one complete inspection	Ave. inspect time (millisecond)
AutoCalibration	104	97	98
HighlightGrabber	22	37	29
DiffuseCatcher	38	52	44

---

[1] Remark: The maximum, minimum, and average inspection time is based on 50 continuous inspections under the same experiment conditions. The average inspection rate equals 1000 / average inspection time (part/sec).

CHAPTER 8

CONCLUSIONS AND FUTURE WORK

8.1 Conclusions

- ☐ In this research study, we have successfully designed a prototype for a low-cost integrated intelligent system for the defect inspection of the specular-coated ceramic tiles on a group of smart cameras. The developed system accurately locates and extracts most of the regular defects, seed defects, and spot defects on the ceramic tiles by the proposed image processing algorithms. The entire inspection process, from the image capture and the image processing to the defect analysis and display is synchronized automatically within the SmartImage cameras in real time. This not only reduces the cost but also saves significant inspection time compared with the traditional inspection systems, which must normally use a frame grabber to transfer digital image data from the camera to a connected PC before any processing takes place.
- ☐ The experimental results on the real test panels demonstrate the effectiveness and robustness of this proposed system
- ☐ The system is low-cost, especially compared to most existing commercial systems; costs for the entire inspection system (illumination and camera) are well under $6,000
- ☐ The results suggest that the designed system is currently adequate to provide a basic substitution for some current simple labor-based surface quality grading and provides a good template for the design of an on-line real-time inspection system for discerning surface defects for many smooth, highly specular coatings.

8.2 Recommendation for future work

- This study has already successfully proposed a method to locate and extract regular defects on specular painted ceramic tiles. With all the information provided, an effective classification method for those defect features will be a good topic for the next stage of research. A schematic plan is shown in Figure 8.1.

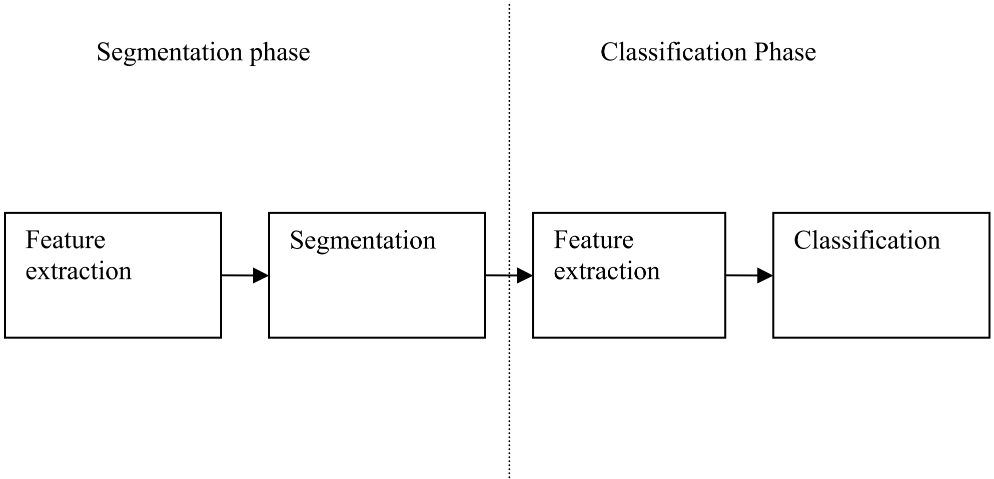

Figure 8.1 A two-stage surface defect classification method

Based upon the results obtained in this study and long-term research goals, the following topics are recommended for further investigation

- Extension of findings presented here to design a suitable real-time automated machine vision system to inspect ceramic tiles with textured surfaces is a good area for future study.
- This study limited its investigation to the inspection on smooth, specular solid paints (i.e., opaque, isotropic coatings that are well-represented by Nayar’s reflectance model). The investigation of other paint formulations, such as metallic paints, which are frequently used on automobile and appliance surfaces, is recommended as a key area for future study.

APPENDIX: A

INTRODUCTION OF SMARTIMAGE INTELLIGENT SENSOR

The purpose of this appendix is to give those readers who are not familiar with DVT SmartImage sensor systems a brief introduction to some of the terms that are mentioned in the contents of this thesis.

A.1 Framework Graphical User Interface

The Framework software is the Graphical User Interface (GUI) that sets up the communication between the user and SmartImage sensor. Firmware is the hardware residing in the SmartImage Sensor that is responsible for all the computations. The users have no direct control of the Firmware. They only program using the Framework, and it then translates all the user commands for the firmware to execute. Figure A-1 shows a simple relationship between the Framework and the firmware.

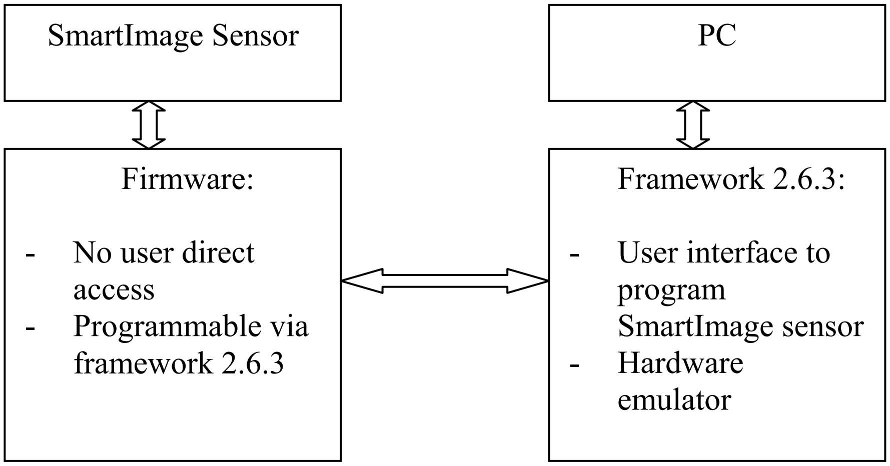

Figure A-1 Relationship between the Framework and the

By using the Framework (version 2.6.3), users set up the connection between a PC and a SmartImage sensor and make changes to the inspection products and system files that are loaded in the SmartImage sensor. During this process, what the Framework user interface does is query the SmartImage sensor for the images and reproduces into the PC what the SmartImage sensor does in its built-in memory with those images. Every image from the SmartImage sensor can be considered as an array of pixels. The image consists of a total of over 300,000 pixels, with 640 columns and 480 rows. As a grayscale system, every pixel provides an intensity value from 0 to 100. An intensity value of 0 corresponds to black, an intensity value of 100 corresponds to white, and others correspond to 99 different shades of gray. Every pixel in the image can be considered a source of information. The SmartImage sensors use this information to inspect the image and provide user feedback such as the presence or absence of a part, flaw detection, code reading, and verification, etc.

Figure B-2 explains the functionality inside the SmartImage sensor. The top system level in figure B-2 controls the overall functionality of the SmartImage sensor such as the I/O configuration and communication setup. At the product level, the user can change the parameter that affects a specific inspection such as illumination and camera exposure time. The SmartImage sensor can be taking the image for the purpose of inspection or simply for the display in the user interface. When it is inspecting the images, it sends out the user-defined output indicating the results of the inspection. Essentially, a product is directly associated with an inspection, so the product parameter affects only one of the inspections that the SmartImage sensor is currently taking. At the bottom sensor level, the user can set some sensor parameters. Softsensors are the working class inside the SmartImage sensors. They are associated with the inspection tasks. Each sensor serves a specific purpose such as locating the part to be inspected or detecting and counting features that make up the part being inspected. The combination of the Softsensor results represents the overall results of each inspection.

A.2 Inspection product and script language

A SmartImage sensor can take images for the purpose of inspection. In a SmartImage sensor system, every *product* defines a specific inspection. When a product is selected as the inspection product, the inspection mode is set to run an inspection in the framework and the SmartImage sensor is triggered; it acquires images and inspects them according to the sensors that the chosen inspection product contains.

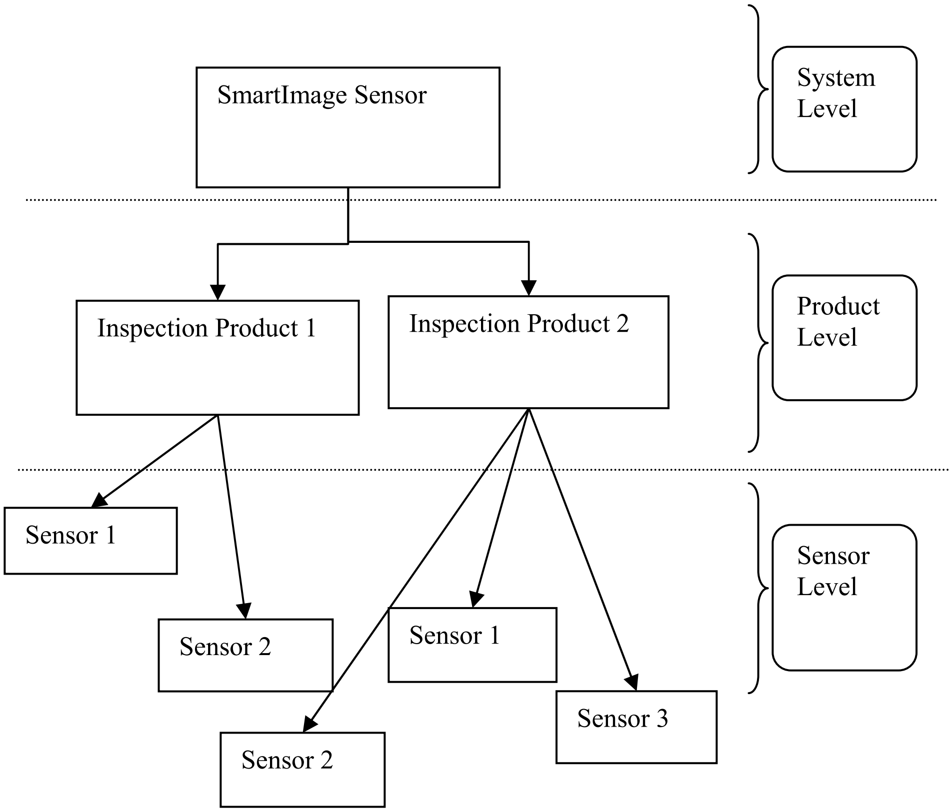

Figure A-2 Hierarchical organization within SmartImage sensor

The DVT Script [34] is a set of programmable tools. It is used to design user customerized inspection products. It can be compiled and executed in the framework and loaded into SmartImage sensor memory to perform specific inspection tasks. A hierarchical organization within the SmartImage sensor with Script shows in figure A-3.

Two types of scripts are available: the background script and the foreground script. Background scripts are created at the system level. They have access to system and product parameters. Common tasks for background scripts are to alter product parameters, trigger inspections, establish communication with external devices, processing image, etc. They run every time the system is powered up. Foreground scripts are created at the product level. They are directly related to the specific inspections. Common tasks for the foreground scripts include gathering data from the Softsensors, performing mathematical and logical calculation, formatting strings to send out of the system via DataLink, etc. They run every time the inspection product that contains them is called to inspect an image.

A.3 SmartLink communications module

DVT's SmartLink communications module, shown in figure A-4, helps us view and analyze multiple inspections from several cameras on the same screen. Using standard Ethernet TCP/IP communication technology, SmartLink was designed to transfer images from up to sixteen networked SmartImage sensors. So it can view multiple inspections at one time with a standard monitor, even without a PC, and transfer them for immediate analysis without any interruption and delay.

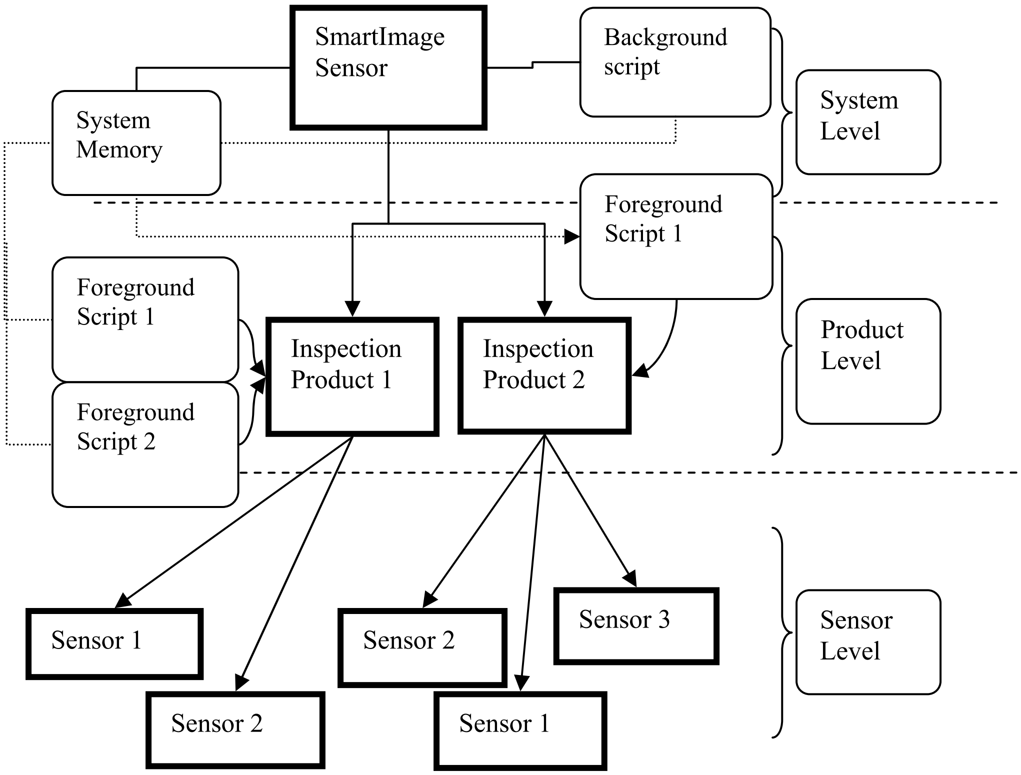

Figure A-3 Hierarchical organization within SmartImage Sensor with script

Figure A-4 DVT SmartLink

APPENDIX: B

CAMERA CALIBRATION AND TSAI'S ALGORITHM FOR CAMERA CALIBRATION

The most commonly used camera calibration method is perhaps the DLT (direct linear transformation) method. But the main problem with the DLT method is that the parameters one obtains from the calibration are not mutually independent from each other. This jeopardizes the orthogonality of the rotation matrix. Actually, this transformation cannot be described perfectly by a perspective transformation because of the distortions that occur between the points on the object and the location of the images of those points. These distortions must be modeled before taking precise measurements. Camera calibration is often taken to include the recovery of the power series coefficients of these distortions. Furthermore, an unknown scale factor in the image sampling may also need to be recovered because the scan lines are typically resampled in the frame grabber, and so the picture cells do not correspond to the discrete sensing elements. Tsai's two-step method for the camera calibration can recover all the information that best fits the measured image coordinates corresponding to the known target point coordinates.

Tsai's camera model is based on the pinhole model of the perspective projection. It relates dimensions in the image frame to the object frame in the Cartesian Space. The model has eleven parameters: five internal (also called intrinsic or interior) parameters,

- f - effective focal length of the pin hole camera,
- k1 - first order radial lens distortion coefficient,
- Cx, Cy - coordinates of center of radial lens distortion -and- the piercing point of the camera coordinate frame's Z axis with the camera's sensor plane,
- sx - scale factor to account for any uncertainty due to the frame grabber horizontal scan line resampling,

And six external (also called extrinsic or exterior) parameters,

- Rx, Ry, Rz - rotation angles for shifting between the world and camera coordinate frames, and
- Tx, Ty, Tz - translation components for shifting between the world and camera coordinate frames.

A target of known geometry is imaged and correspondences between these target points and their images are obtained. These form the basic data on which the calibration is based. Tsai's method first tries to obtain estimates of as many parameters as possible, using linear least squares fitting methods. In this stage, all extrinsic parameters except T_z are estimated from an over-determined set of linear equations with five unknowns, using the method of Least Squares. In the subsequent step, the rest of the parameters are obtained using a nonlinear optimization method that finds the best fit between the observed image points and those predicted from the target model.

As for this application, Jean-Yves Bouquet's *Camera Calibration Toolbox for Matlab* is used in the earlier stage and finally refers to a two-stage algorithm introduced from the reference [32] for the coplanar calibration

APPENDIX: C

TEST PANEL IMAGES AND THEIR INSPECTION RESULTS

This appendix includes all the experiment data collected from seven test ceramic tiles. The data of each panel is organized in such a way:

1. Images: from the upper left to the lower right they are the original diffuse image, the diffuse image with marked dark blobs, the diffuse image with marked white blobs, the diffuse image with ellipse fitting, and the specular image with marked highlight spots
2. Tables: Four different tables are used to completely describe the collected defect information of every single inspection product. The first table gives the real world physical location of defects extracted from the diffuse image. The data transformed from calibration and the data from the real measurement with high precision digital ruler are compared. The second table lists all the information on the defect feature shape such as the area, bounding box width and height, convexity, compactness, and perimeter from the same diffuse image. The third table gives the defect information extract from eclipse fitting algorithm as mentioned from the chapter Four. The last table gives the highlights information from the specular image such as physical location, area, etc.

Results of the test panel C have been used as an example in chapter seven. So only the image results of the test panel C are listed in this appendix. The table data will not be repeated here again. Readers can refer to chapter seven to get that table data if necessary.

Test Panel A

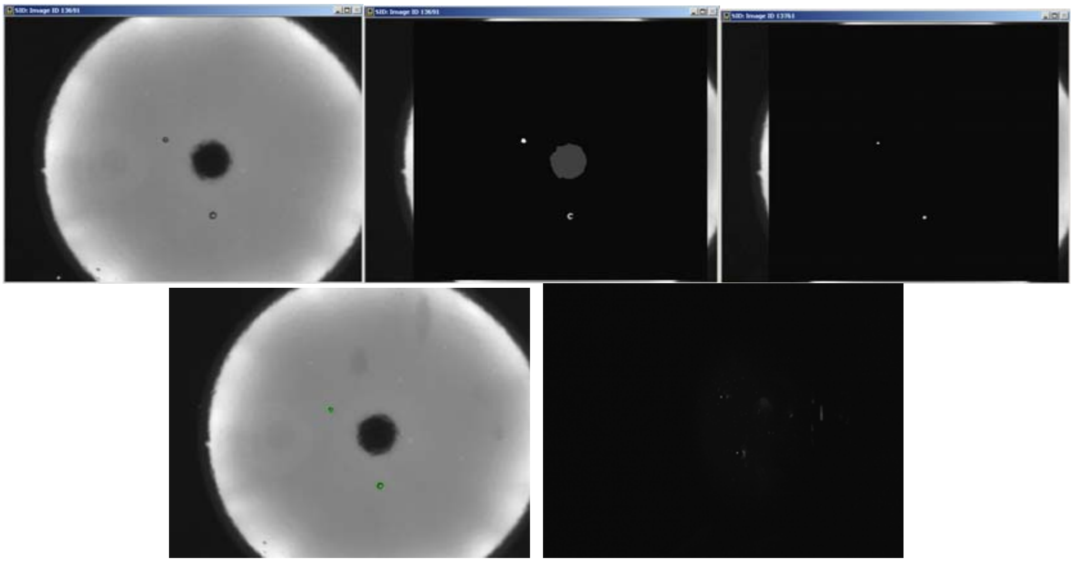

Figure C-A Images from inspection results of test panel A

Table C-A1 Inspection results of test panel A I

Feature index	Measured x position (millimeter)	Measured y position (millimeter)	Calibrated x position (millimeter)	Calibrated y position (millimeter)	Absolute error in x	Absolute error in y.
1	70.8	87.2	70.8	87.3	0.0	0.1
2	87.3	61.2	87.0	61.6	0.3	0.4

Table C-A2 Inspection results of Test Panel A II

Defect index	Darkblob Area (pixel)	Boundingbox Width (pixel)	Boundingbox Height (pixel)	Convexity	Compactness	Peripheral	Whiteblob Area (pixel)
1	44	8	7	0.84	0.76	27	12
2	52	10	11	0.49	0.29	48	31

Table C-A3 Inspection results of test panel A III

Defect index	Center x (pixel)	Center y (pixel)	Boundingbox height (pixel)	Boundingbox width (pixel)	angle	Area (pixel)
1	286	215	9	12	16.2	84.8
2	374	351	13	14	330.2	143.0

Table C-A4 Inspection results of test panel A IV

Highlight	Area (pixel)	Center x (millimeter)	Center y (millimeter)	Distance (millimeter)
1	2	69.8	88.1	1.3
2	3	85.6	63.2	2.1

Test panel B

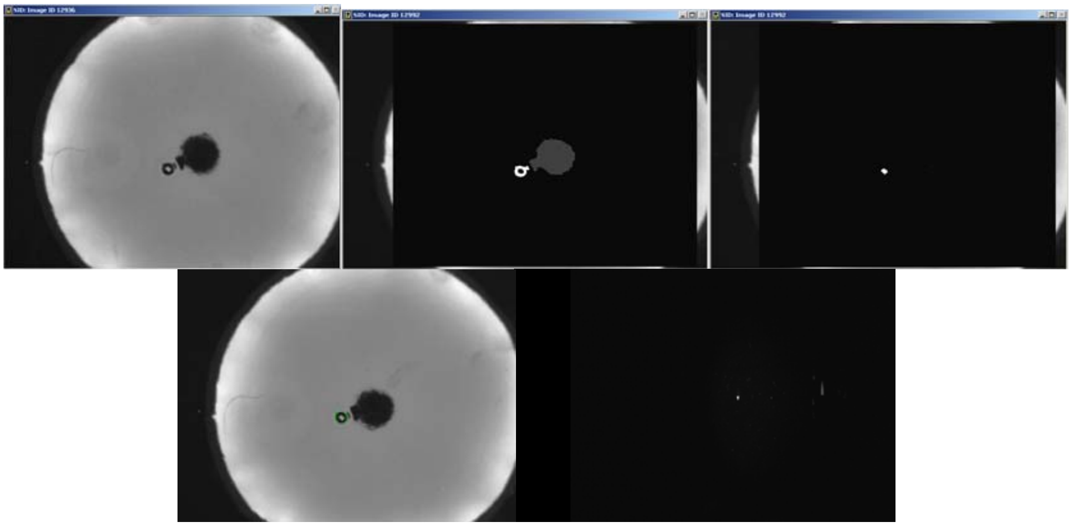

Figure C-B Images from inspection results of test panel B

Table C-B1 Inspection results of test panel B I

Feature index	Measured x position (millimeter)	Measured y position (millimeter)	Calibrated x position (millimeter)	Calibrated y position (millimeter)	Absolute error in x	Absolute error in y.
1	75.1	74.9	75.4	75.2	0.3	0.3

Table C-B2 Inspection results of test panel B II

Defect index	Darkblob Area (pixel)	Boundingbox Width (pixel)	Boundingbox Height (pixel)	Convexity	Compactness	Peripheral	Whiteblob Area (pixel)
1	365	27	21	0.64	0.35	115	68

Table C-B3 Inspection results of test panel B III

Defect index	Center x (pixel)	Center y (pixel)	Boundingbox height (pixel)	Boundingbox width (pixel)	angle	Area (pixel)
1	309	280	22	25	29.9	432.0

Table C-B4 Inspection results of test panel B IV

Highlight	Area (pixel)	Center x (millimeter)	Center y (millimeter)	Distance (millimeter)
1	2	77.3	75.9	2.0

Test panel C

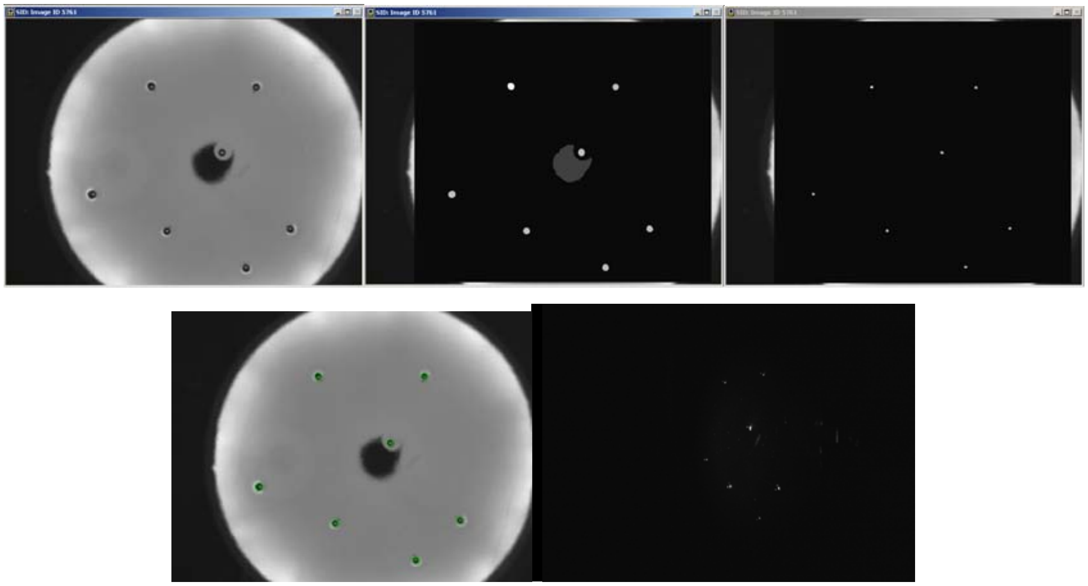

Figure C-C Images from inspection results of test panel C

Test panel D

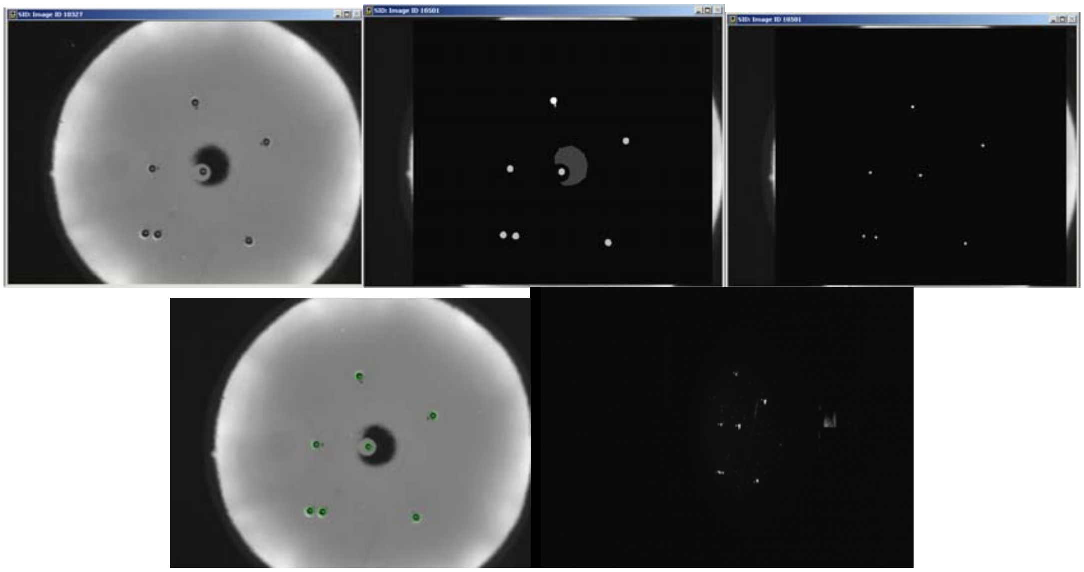

Figure C-D Images from inspection results of test panel D

Table C-D1 Inspection results of test panel D I

Feature index	Measured x position (millimeter)	Measured y position (millimeter)	Calibrated x position (millimeter)	Calibrated y position (millimeter)	Absolute error in x	Absolute error in y.
1	80.3	100.7	80.2	101.9	0.1	1.2
2	104.7	88.2	105.0	88.5	0.3	0.3
3	66.2	78.6	65.6	79.0	0.6	0.4
4	83.4	77.6	83.1	78.1	0.3	0.5
5	64.0	56.3	63.3	56.4	0.7	0.1
6	68.1	56.1	67.5	56.1	0.6	0.0
7	99.2	54.1	99.3	53.9	0.1	0.2

Table C-D2 Inspection results of test panel D II

Defect index	Darkblob Area (pixel)	Boundingbox Width (pixel)	Boundingbox Height (pixel)	Convexity	Compactness	Peripheral	Whiteblob Area (pixel)
1	115	11	17	0.62	0.60	49	10
2	105	11	12	0.86	0.84	40	10
3	112	12	12	0.90	0.84	41	13
4	111	11	12	0.86	0.87	40	14
5	118	12	12	0.96	0.88	41	9
6	120	12	13	0.90	0.84	42	11
7	111	12	12	0.84	0.83	41	11

Table C-D3 Inspection results of test panel D III

Defect index	Center x (pixel)	Center y (pixel)	Boundingbox height (pixel)	Boundingbox width (pixel)	angle	Area (pixel)
1	335	138	13	13	329.4	132.7
2	466	209	12	13	83.0	122.5
3	259	260	12	13	87.3	122.5
4	351	264	13	13	106.3	132.7
5	248	378	13	13	333.8	132.7
6	270	380	13	14	316.4	143.0
7	436	389	13	13	26.7	132.7

Table C-D4 Inspection results of test panel D IV

Highlight	Area (pixel)	Center x (millimeter)	Center y (millimeter)	Distance (millimeter)
1	4	80.7	99.9	2.1
2	15	104.3	87.4	1.3
3	5	64.5	78.8	1.1
4	16	82.1	77.8	1.0
5	4	65.7	56.9	2.5
5	4	65.7	56.9	2.0
7	10	98.1	55.1	1.7

Test Panel E

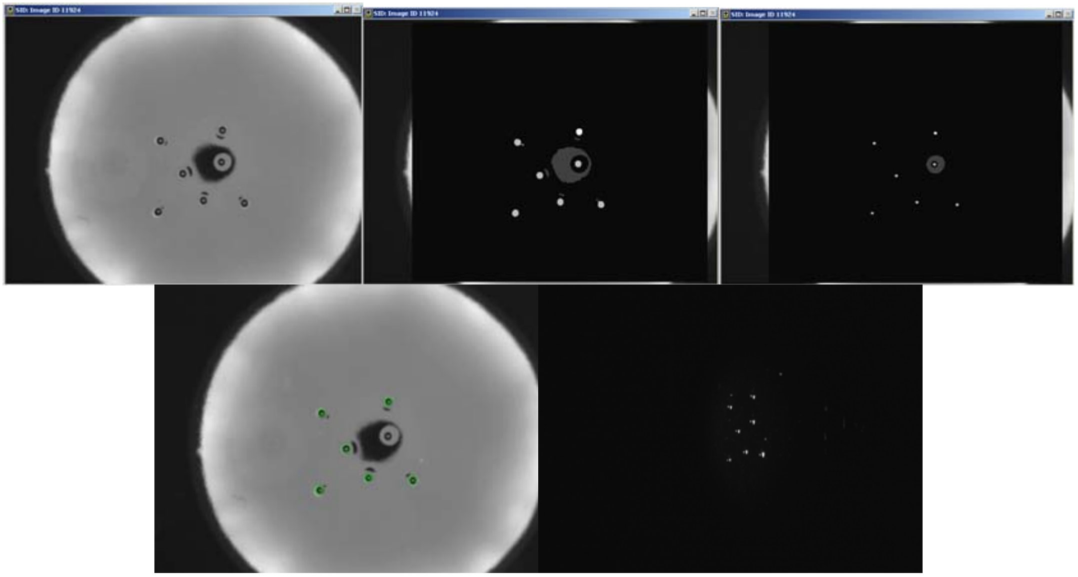

Figure C-E Images from inspection results of test panel E

Table C-E1 Inspection results of test panel E I

Feature index	Measured x position (millimeter)	Measured y position (millimeter)	Calibrated x position (millimeter)	Calibrated y position (millimeter)	Absolute error in x	Absolute error in y.
1	90.2	91.0	90.4	91.4	0.2	0.4
2	69.5	87.2	69.2	87.8	0.3	0.6
3	90.0	80.3	90.0	80.6	0.0	0.3
4	77.1	76.2	76.9	76.6	0.2	0.4
5	83.9	67.3	83.9	67.4	0.0	0.1
6	97.6	66.4	98.0	66.4	0.4	0.0
7	68.9	63.2	68.5	63.5	0.4	0.3

Table C-E2 Inspection results of test panel E II

Defect index	Darkblob Area (pixel)	Boundingbox Width (pixel)	Boundingbox Height (pixel)	Convexity	Compactness	Peripheral	Whiteblob Area (pixel)
1	107	11	12	0.80	0.86	40	14
2	115	11	13	0.80	0.84	42	14
3	113	11	12	0.82	0.87	40	12
4	114	11	12	0.86	0.89	40	14
5	113	12	13	0.85	0.81	42	13
6	109	11	12	0.82	0.83	41	11
7	119	12	12	0.89	0.84	42	10

Table C-E3 Inspection results of test panel E III

Defect index	Center x (pixel)	Center y (pixel)	Bounding box height (pixel)	Boundingbox width (pixel)	angle	Area (pixel)
1	389	194	13	13	34.3	132.7
2	278	213	13	13	71.8	132.7
3	388	251	13	13	88.2	132.7
4	319	272	13	14	7.7	143.0
5	356	321	13	13	68.0	132.7
6	430	325	13	14	97.3	143.0
7	274	341	13	13	125.7	132.7

Table C-E4 Inspection results of test panel E IV

Highlight	Area (pixel)	Center x (millimeter)	Center y (millimeter)	Distance (millimeter)
1	8	91.9	89.9	2.1
2	8	71.8	87.8	2.6
3	12	91.5	79.8	1.7
4	8	78.5	76.1	1.7
5	10	85.6	67.4	1.7
6	20	99.4	66.7	1.4
7	4	70.4	63.7	1.9

Test Panel F

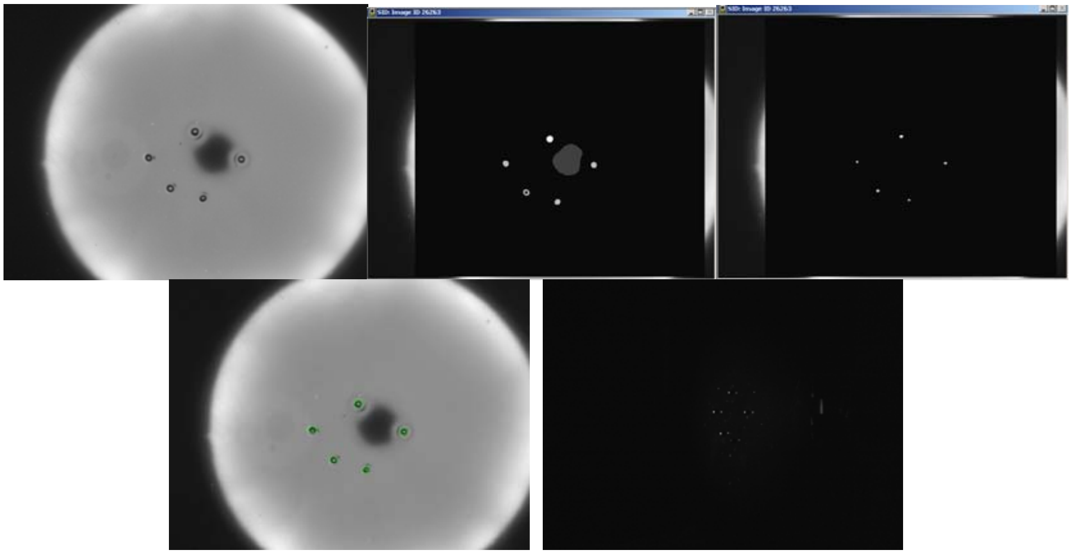

Figure C-F Images from inspection results of test panel F

Table C-F1 Inspection results of test panel F I

Feature index	Measured x position (millimeter)	Measured y position (millimeter)	Calibrated x position (millimeter)	Calibrated y position (millimeter)	Absolute error in x	Absolute error in y.
1	79.8	85.9	80.0	86.3	0.2	0.4
2	64.8	77.6	64.6	77.8	0.2	0.2
3	94.9	77.0	95.5	77.1	0.6	0.1
4	71.7	67.7	71.7	67.7	0.0	0.0
5	82.5	64.4	82.6	64.3	0.1	0.1

Table C-F2 Inspection results of test panel F II

Defect index	Darkblob Area (pixel)	Boundingbox Width (pixel)	Boundingbox Height (pixel)	Convexity	Compactness	Peripheral	Whiteblob Area (pixel)
1	118	12	12	0.95	0.88	41	26
2	97	11	11	0.82	0.81	39	15
3	96	11	12	0.92	0.79	39	21
4	79	12	11	0.78	0.31	57	26
5	87	11	10	0.75	0.81	37	14

Table C-F3 Inspection results of test panel F III

Defect index	Center x (pixel)	Center y (pixel)	Boundingbox height (pixel)	Boundingbox width (pixel)	angle	Area (pixel)
1	335	221	13	14	328.2	143.0
2	255	266	11	17	1.6	146.9
3	416	269	12	14	2.6	132.0
4	292	320	12	14	39.5	132.0
5	349	337	11	13	319.6	112.3

Table C-F4 Inspection results of test panel F IV

Highlight	Area (pixel)	Center x (millimeter)	Center y (millimeter)	Distance (millimeter)
1	2	77.8	86.9	2.3
2	4	66.3	78.4	1.8
3	1	101.1	86.0	4.9
4	3	92.0	77.8	
5	4	69.5	68.6	2.4
6	1	87.6	66.0	5.3

Test Panel G

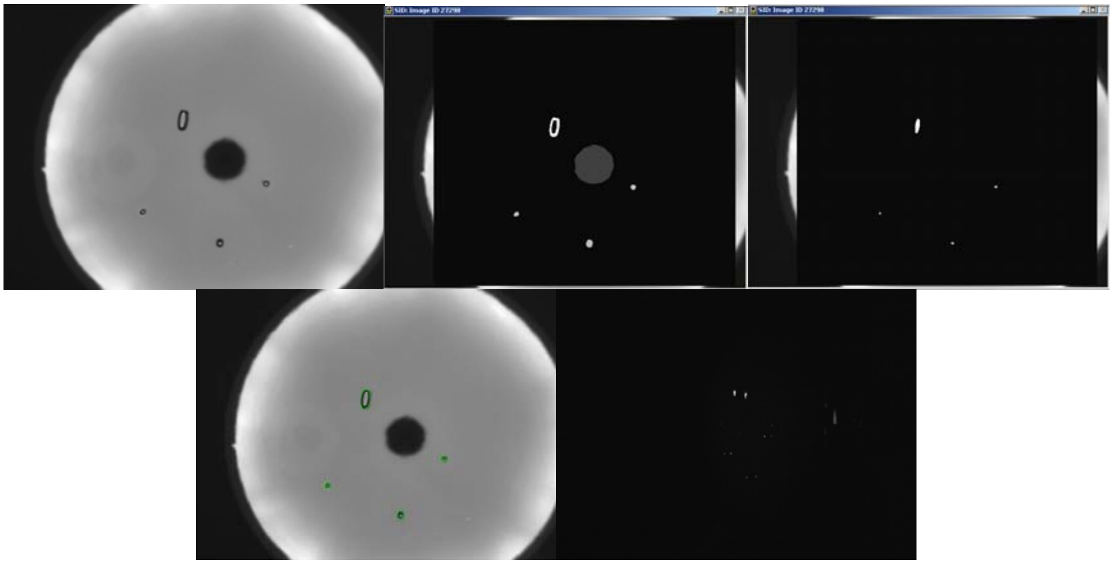

Figure C-G Images from inspection results of test panel G

Table C-G1 Inspection results of test panel G I

Feature index	Measured x position (millimeter)	Measured y position (millimeter)	Calibrated x position (millimeter)	Calibrated y position (millimeter)	Absolute error in x	Absolute error in y.
1	74.0	91.1	73.5	91.3	0.5	0.2
2	60.9	62.3	60.3	62.2	0.6	0.1
3	85.0	52.2	85.1	52.0	0.1	0.2
4	99.5	71.1	99.9	71.1	0.4	0.0

Table C-G2 Inspection results of test panel G II

Defect index	Darkblob Area (pixel)	Boundingbox Width (pixel)	Boundingbox Height (pixel)	Convexity	Compactness	Peripheral	Whiteblob Area (pixel)
1	326	18	34	0.26	0.18	150	161
2	60	9	8	0.58	0.84	30	12
3	132	12	14	0.70	0.84	45	19
4	68	9	9	0.97	0.84	32	18

Table C-G3 Inspection results of test panel G III

Defect index	Center x (pixel)	Center y (pixel)	Bounding box height (pixel)	Bounding box width (pixel)	angle	Area (pixel)
1	300	194	18	37	98.0	523.1
2	440	300	11	12	14.2	103.7
3	233	348	10	11	331.1	86.4
4	362	400	13	14	83.7	143.0

Table C-G4 Inspection results of test panel G IV

Highlight	Area (pixel)	Center x (millimeter)	Center y (millimeter)	Distance (millimeter)
1	17	70.1	91.6	2.2
2	13	81.3	90.1	
3	1	62.9	63.6	3.0
4	1	91.3	54.4	6.7
5	1	98.6	71.9	1.5

REFERENCES

1. R. Lambourne, “Paint and Surface Coatings”, *Theory and Practice*, Ellis Horwood Ltd., 1987
2. Frank Chen, Gordon M. Brown, Mumin Song, “Overview of three-dimensional shape measurement using optical methods”, *Optical Engineering*, Jan. 2000, 10-22
3. American National Standards Institute, “ANSI 137.1 standard for ceramic tile”, 1988
4. B. K. P. Horn, “Shape from shading: a method for obtaining the shape of a smooth opaque object from one view”, *MIT Project MAC Int. Rep.* TR-79 and *MIT AI Lab. Tech. Rep.* 232, Nov. 1970
5. B. K. P. Horn, “ Hill shading and the reflectance map”, *Proc. IEEE*, vol. 69, no. 11, 14-47, Jan. 1981
6. R. J. Woodham, “Photometric stereo: A reflectance map technique for determining surface orientation from image intensity”, *Proc. SPIE*, vol. 155, 136-143, 1978
7. J. H. Lambert, “Photometria sive de mensura de gratibus luminis, colorum et umbrae”, *Augsberg, Germany: Eberhard Klett,* 1760
8. B. Phong, “Illumination for computer generated pictures”, *Communication ACM*, vol. 18, 311-317, 1975
9. K. Ikeuchi, “Determining surface orientations of specular surfaces by using the photometric stereo method”, *IEEE Trans. Pattern Analysis Machine Intelligence,* vol. 3, no. 6, 661-669, Nov. 1981
10. A. C. Sanderson, L. E. Weiss, S. K. Nayar, “Structured highlight inspection of specular surfaces”, *IEEE Trans. Pattern Analysis Machine Intelligence*, vol. 10, no.1, 44-55, Jan. 1988
11. Glenn Healey, Thomas Binford, “Local shape from specularity”, *Computer Vision, Graphics, and Image Processing*, 62-86, 1988
12. K. Torrance, E. Sparrow, “Theory for off-specular reflection from roughened surfaces”, *Journal of the Optical Society of America*, 57:1105-1114, Sep. 1967
13. S. K. Nayar, Katsushi Ikeuchi, Takeo Kanade, “Surface Reflection: Physics and Geometrical Perspectives”, *IEEE Trans. On Pattern Analysis and Machine Intelligence*, vol. 13, no. 7, 611-634, July 1991
14. Johné M. Parker, et al., “Inspection Technology to Facilitate Automated Quality Control of Highly Specular, Smooth Coated Surfaces”, *Proceedings of the 2002 IEEE International Conference on Robotics and Automation,* 2002
15. R. L. Reynolds, et al., “Theory and applications of a surface inspection technique using double-pass retrospection”, *Optical Engineering*, 32(9): 2122-2129, 1993
16. D. Pe´rard and J. Beyerer, ‘‘Three-dimensional measurement of specular free-form surfaces with a structured-lighting reflection technique,’’ *Proceedings of SPIE* Vol. 3204, 1997
17. P. S. Huang, Q. Hu, F. Jin, and F.P. Chiang, ‘‘Color-encoded digital fringe projection technique for high speed three-dimensional surface contouring,’’ *Optical. Engineering*. 38(6)**,** 1065–1071, 1999

18. Roland Höfling, Petra_Aswendt, and Reimund Neugebaue, “Phase reflection—a new solution for the detection of shape defects on car body sheets”, *Optical Engineering,* 39, pp.175-182, 2000
19. Stefan Karbacher *et al.*, “Visualization and detection of small defects on car-bodies”, *Vision, Modeling and Visualization 99’*, 1-8, 1999
20. R. L. Reynolds, *et al.*, “Theory and applications of a surface inspection technique using double-pass retrospection”, *Optical Engineering*, 32(9):2122-2129, 1993
21. DU PONT, “Dupont Training Program Workbook”, 1993
22. Bellver-Cebreros, M. Rodriguez-Danta, “Caustics and the Legendre Transform”, *Optics Communications*, 92(4-6): 187-192, 1992
23. Lai, T. and Parker, J. M. “Vision system design for on-line quality control of highly specular coated surfaces.” *In Mechatronics and Machine Vision (Ed. J. Billingsley),* 2000 (Research Studies Press)
24. J. Parker, , P. Gnanaprakasam, S. Ganapathiraman, Z. Hou,, “Efficient 3-D Characterization of Surface Defects in Smooth Specular Coatings”, *Proc. Advanced Intelligent Mechatronics* 2005,
25. J. Canny**, “***A Computational Approach to Edge Detection”*, *IEEE Transactions on Pattern Analysis and Machine Intelligence,* Vol. 8, No. 6, Nov. 1986
26. A. Rosenfeld, E. Johnston, “Angle Detection on Digital Curves*”*, *IEEE Trans. Computers*, 22:875-878, 1973.
27. C.H.Teh, R.T.Chin, “On the Detection of Dominant Points on Digital Curves”, *IEEE Tr. PAMI*, 1989, v.11, No.8, p. 859-872.
28. Andrew W. Fitzgibbon, R. B. Fisher, “A Buyer’s Guide to Conic Fitting”, *Proc.5th British Machine Vision Conference*, Birmingham, pp. 513-522, 1995.
29. Zhengyou Zhang, “Parameter Estimation Techniques: A Tutorial with Application to Conic Fitting”, *Image and Vision Computing Journal*, 1996
30. Jukka Iivarinen, Markus Peura, Jaakko Srel, and Ari Visa, “Comparison of Combined Shape Descriptor for Irregular Objects” *8th British Machine Vision Conference,* 1997
31. Pradeep Gnanapraksam, “Characterization of seed defects in highly specular smooth coated surfaces”, *Master thesis at University of Kentucky*, 2004
32. Tsai, Roger Y. “An efficient and accurate camera calibration technique for 3D machine vision**”***, IEEE Journal of Robotics and Automation,* Vol. RA-3, No. 4, 323-344, August 1987
33. DVT Corporation, “DVT SmartImage Sensor installation and user guide”, 7th edition, 2003
34. DVT Corporation, “DVT script reference manual”, 4th edition, 2003
35. Johné M. Parker, “An analytical and experiment investigation of physically accurate synthetic images for machine vision design”, *Doctoral thesis of Georgia Institute of Technology* , 1996
36. “ Method and system for processing measurement signals to obtain a value for a physical parameter”, United States Patent, No. 6,092,419: filed November 21, 1997; granted July 25, 2000
37. “Method and system for measuring a physical parameter of at least one layer of a multi layer article without damaging the article and sensor head for use therein”, United States Patent, No. 6,128,081: filed November 27, 1997; granted October 3, 2000

VITA

Jinhua Li was born on 5th November, 1978 in Tianjin, China. He received his Bachelor's Degree in Automation from University of Science and Technology of China, in Hefei, Anhui province, China in the year 2001. In pursuit of his higher education, he matriculated at the College of Engineering at the University of Kentucky, in Lexington.